Electronic Supplementary Information for:

Bifunctional Water-Electrolysis-Catalysts Meeting Band-Diagram Analysis: Case-Study of "FeP" Electrodes

Rashad Ali,[#,a] Aixian Shan,[#,b] Govidarajan Saranya,[#,c] Xian Jian,*[,a] Asif Mahmood,[d] Nasir Mahmood,[e] Mingyang Chen,*[,c] Yunguo Yang,[b] Woon-Ming Lau*[,b,f]

[a]*School of Materials and Energy, University of Electronic Science and Technology of China, Chengdu, 611731, China*
Email. jianxian@uestc.edu.cn
[b]*Advanced Innovation Center of Materials Genome Engineering; Center for Green Innovation, School of Mathematics and Physics, University of Science and Technology Beijing, Beijing 100083, China*
Email. leolau@ustb.edu.cn
[c]*Shunde Graduate School of University of Science and Technology Beijing, Foshan 528000, China; Center for Green Innovation, School of Materials Science and Engineering, University of Science and Technology Beijing, Beijing 100083, China; Beijing Computational Science Research Center, Beijing 100193, China*
Email. mychen@ustb.edu.cn
[d]*School of Chemical and biomolecular Engineering, The University of Sydney, 2006, Sydney, Australia*
[e]*School of Engineering, RMIT University, 124 La Trobe Street, 3001 Melbourne, Victoria, Australia*
[f]*Institute of Fundamental and Frontier Science, University of Electronic Science and Technology of China, Chengdu, 610054, China*
Email. leolau@ustb.edu.cn

[#]These authors contributed equally to this work.
*Correspondence and request for materials should be addressed to X.J (email: jianxian@uestc.edu.cn) or M.C (email: mychen@ustb.edu.cn) or W.M.L (email: leolau@ustb.edu.cn)

1. Survey of Relevant Prior Arts

A survey of relevant prior arts is shown in **Table S1** as follows (if not specified, electrolyte is 1 M KOH):

Nominal Catalyst	reported $V_{10,\ fuel\ cell}$ (V)	reported $\eta_{10,\ HER}$ (mV)	reported $\eta_{10,\ OER}$ (mV)	$\eta_{10,\ HER+OER}$ (mV)	1.23 V + $\eta_{10,\ HER+OER}$ (V)	Work-function (eV)	**Ref.**
Nano-FeP@NF	1.40	56	90	146	1.376	ex-situ 4.7; cathode-flatband voltage at 0.02V relative to RHE	this work
Self-Supported N-Co_3O_4@C Nanomeshes	1.40	42	96	138	1.368	-----	S[1]
FeP/Ni_2P@NF	1.42	14	154	168	1.40	-----	S[2]
$VSxO_{2-x}$/Ni_2S_3@NF	1.42	100	150	250	1.48	-----	S[3]
Ni_2S_3@NF	-----	170	340	510	1.74	-----	S[3]
VS_xO_{2-x}	-----	150	360	510	1.74	-----	S[3]
FeCoNi/MoS/NF	1.43	58	184	242	1.47	-----	S[4]
NiCo/NF/ graphiyne	1.43	43	216	259	1.49	-----	S[5]
$NiFe(OH)_2$/ graphene@NF	1.43	70	130	200	1.43	-----	S[6]
CoP@Ti_3C_2 3D MXene-Based Architecture	1.565	168	220	388	1.619	-----	S[7]
Colloidal CoP Nanocrystals	1.56	62.5 (CoP)	280 (Co_2P)	342.5	1.572	-----	S[8]
O-CoS_2−MoS_2 (O-CoMoS) HNSts	1.6	97	272	369	1.6	-----	S[9]
Co-P-derived films	-------	94	345	439	1.67	-----	S[10]
Nanostructured Ni_5P_4 films	1.7	150	290	440	1.67	-----	S[11]
MoP@RGO CoP@RGO	1.6	93 MoP	280 (CoP)	370	1.6	-----	S[12]
$NiCo_2O_4$ MCbds	1.65	110	290	400	1.63	-----	S[13]
Fe-Doped CoP nanoarray	-----	78	-----	-----	-----	-----	S[14]
$NiCo_2S_4$ NW/NF	1.63	210	260	470	1.7	-----	S[15]
A-Ni@GC	-----	34	-----	-----	-----	-----	S[16]
FeCoP NSts @CNTBs	1.5	76 CoP@CNT	243 $Co_{0.7}Fe_{0.3}P$/ CNT	319	1.55	-----	S[17]
CoP/NCNHP	1.64	115	310	425	1.655	-----	S[18]
Bimetallic nanohybrids@ MOF	1.60	89 CF@FeCoP/ NC	228 CF@FeCoS/ NC	317	1.55	-----	S[19]

Fe-doped CoP	1.49	78	190	268	1.5	-----	S[20]
Multi-elements $FeCoNiP_xS_y$	1.46	43 FeCoNiS	258 at 100mA/cm^2 $FeCoNiP_{0.5}S_{0.5}$	301	1.53	-----	S[21]
Ag@Co_xP NPs	-----	-----	310	-----	-----	-----	S[22]
Pt@$Co(OH)_2$ nanosheet arrays	-----	32	-----	-----	-----	-----	S[23]
3D porous Ni/Ni_8P_3	1.61	130	270 at 30mA/cm^2	400	1.63	-----	S[24]
FePx/Fe–N–C/NPC	1.58	75 H_2SO_4	325	400	1.63	-----	S[25]
FeP NPs	1.59	165	227	392	1.59	-----	S[26]
FeP powder	-----	185	-----	-----	-----	-----	S[27]
Fe/P/C	------	256 (H_2SO_4)	330	586	1.82	-----	S[28]
Defected FeP	------	108 (KOH) 65 (H_2SO_4)	------	-----	-----	-----	S[29]
FeP NPs	-----	-----	260	-----	-----	-----	S[30]
FeP@NPCs	-----	-----	300	-----	-----	-----	S[31]
FeP nanorods	-----	120 H_2SO_4	-----	-----	-----	-----	S[32]
CoP nano-rods array	1.62	54	290	344	1.574	-----	S[33]
Porous MoO_2 nanosheets	1.53	27	260	287	1.517	-----	S[34]
MoS_2/Ni_3S_2 heterostructures	1.56	110	218	328	1.56	-----	S[35]
CoSe/NiFe layered-double-hydroxide nanosheets	1.71	260	250	510	1.74	-----	S[36]
CoP_2 nanoparticles	1.56	88	300	388	1.618	-----	S[37]
Cu nanowires/ $NiFe(OH)_2$ nanosheets	1.54	116	199	315	1.545	-----	S[38]
$Co_{0.6}Fe_{0.4}P$ nanoframes	1.57	133	298	431	1.661	-----	S[39]
CoP (MoP)-$CoMoO_3$@CN nanocomposite	1.55	198	296	494	1.726	-----	S[40]
Co_1Mn_1CH/NF	1.68	180	294	474	1.7	-----	S[41]
SILAR deposited iron phosphate	1.67	157	230	384	1.614	-----	S[42]
NiCoFe LTHs/CFC	1.55	200	239	439	1.67	-----	S[43]
CoP Nanobush	1.85	252	380	632	1.86	-----	S[44]
Ni_2P/rGO	1.61	142	260	402	1.63	-----	S[45]

As shown in this survey, the bifunctional cell-voltage of 1.40 V shown in the present work compares well with all prior relevant results. Although some prior works show HER overpotentials lower than that in the present work, all bifunctional cell-voltages in the literature are not less than 1.40 V.

2. Details in Experiments

Chemicals: Pt/C (20 wt%, Macklin), Nafion (5 wt %, Aldrich Chemistry), potassium hydroxide (AR, KESHI), sodium dihydrogen phosphate (AR, KESHI), sodium sulphate anhydrous (AR, KESHI), iron chloride hexahydrate (AR, KESHI), sodium hypophosphite monohydrate (AR, KESHI), ruthenium oxide hydrate (AR, Aladdin) and nickel foam were bought from commercial companies and used without further purification.

Synthesis of nano-FeP: Nano-α-Fe_2O_3 precursor particles were synthesized by a hydrothermal treatment of $FeCl_3{\cdot}6H_2O$ with NaH_2PO_4 and Na_2SO_4. Specifically, 259.53 mg $FeCl_3{\cdot}6H_2O$, 1.66 mg NaH_2PO_4 and 6.25 mg Na_2SO_4 were dissolved in 80 mL of deionized water. The solution was placed into a Teflon-lined stainless-steel autoclave for a hydrothermal treatment at 220 ºC for 40 h. Upon cooling, the samples were collected and dried in air at 80 ºC. The phosphidation of nano-α-Fe_2O_3 was conducted in a tube furnace at 400 ºC for 2 h with $NaH_2PO_2{\cdot}H_2O$ as the phosphorus source and argon as the carrier gas. In the process of engineering the best nano-FeP for low-voltage and stable water-electrolysis, the relative amount of $NaH_2PO_2{\cdot}H_2O$ in reference to the amount of nano-α-Fe_2O_3, was tuned (details summarized in **Table S2**).

Preparation of Nickel foam electrodes:

The commercial nickel foam was cut into (1 cm*1 cm) electrodes and washed subsequently in sonicator with HCl solution (5 mL HCl into 175 mL DI water) for 10 min, deionized water for 15 min and absolute ethanol for 7 min with rinsing. Finally, electrodes were dried by air drier.

Preparation of Ink:

The resultant nano-FeP was mixed with carbon black (4:1 by weight) in ethanol to form an ink slurry which was loaded onto nickel-foam with Nafion as a binder. Bifunctional cells were then formed with such loaded nickel foam electrodes.

Characterization: The as-obtained products of α-Fe_2O_3 and FeP nano-rings were studied by field emission scanning electron microscopy (SEM) with an "FEI Inspect-F" SEM, transmission electron microscopy (TEM) with an "JEOL JEM-7600F" TEM, high-resolution transmission electron microscopy (HRTEM) with an "FEI-F200" HRTEM, and powder X-ray diffraction (XRD) with an XRD-7000X instrument. Electrochemical measurements were conducted using an electrochemical workstation of CHI 760E. X-ray photoelectron spectroscopy (XPS) and ultraviolet photoelectron spectroscopy (UPS) were performed with a "PHI 5000 VersaProbe III" instrument.

Electrochemical Characterization: Electrochemical measurements were conducted using a typical three-electrode system for HER and OER and a two-electrode setup for overall water-splitting in 1 M KOH. All measurements were conducted at room temperature. An Ag/AgCl electrode was used as the reference electrode, and Pt and graphite were used as the counter electrodes, with catalyst-loaded nickel-foam forming the working electrode. Linear sweep voltammetry (LSV) was adopted to record the polarization curves at a scan rate of 5 mV/s. Long-term durability was determined by the amperiometric i-t technique at an applied voltage of 0.32 V vs Ag/AgCl, -1.052 V vs Ag/AgCl and 1.5 V for OER, HER and overall water splitting, respectively. The electrochemical surface area (ECSA) measurements were recorded by running the standard cyclic voltammetry (CV) scans in a voltage range of 0.03 to 0.13 V and -0.945 to -0.845 V for OER and HER, respectively. The electrochemical impedance spectroscopic (EIS) measurements were taken in a frequency range of 100 kHz - 0.01 Hz. The Impedance-Potential (IMPE) method was used to calculate the flat band potential at a

frequency of 1000 Hz. The uncompensated resistance value for each electrode in the electrolyte solution was measured before testing. All the potentials shown here were referenced to reversible hydrogen electrode (RHE).

3. **Details in Computations:**

All of the first-principles calculations were performed using the Vienna Ab Initio Simulation Package (VASP) with the projector-augmented-wave (PAW) potentials. The structure optimization calculations were performed with the pure Perdew–Burke–Ernzerhof exchange-correlation functional. Dispersion corrections were included using the DFT-D3 methods. The 8×8×8, 8×8×8, 2×2, and 2×2 Monkhorst-Pack meshes were adopted for the bulk FeP, bulk $FePO_4$, FeP (010) slab, and $FePO_4$ (010) slab, respectively, and Γ-only calculation was performed for the heterojunction system. For the bulk systems, the equilibrium geometries were fully optimized with both the lattice vectors and atom coordinates relaxed with the tolerance less than 0.01 eV/Å on each atom. For the slab calculations, a vacuum of 15 Å was used to separate the slab and its periodic images; the lattice vectors are fixed and the atom coordinates are fully relaxed using a convergence criterion of 0.01 eV/Å on each atom. The single-point calculations were carried out for the optimized structures with the hybrid HSE06 functional to generate wave functions used in the electronic structure analyses, such as density of states (DOSs) analysis and work-function determination.

The surface-oxidized nanostructure of FeP ($FePO_4$/FeP) was modelled with a heterojunction model comprised of a FeP-2[46] slab and an α-quartz $FePO_4$ slab.[47] Among the different slab stacking configurations, the stacking between the FeP (010) surface and the O-polar $FePO_4$ (010) surface by aligning the (010) direction of FeP and the y direction of $FePO_4$, exhibits small lattice mismatch and strong interfacial binding, and is therefore chosen for the modelling of $FePO_4$/FeP. The FeP (010) slab supercell is a 2×3×2 cut from the optimized bulk

FeP structure with 48 FeP units, whereas the $FePO_4$ slab supercell is a 2×2×1 cut with 12 $FePO_4$ units. The area of the 2×2 FeP (010) surface is 10.2×11.4 $Å^2$, and the area of the 2×1 $FePO_4$ (010) surface is 10.1×11.2 Å. According to the experiment, the $FePO_4$ layer is ultrathin (~2 nm), and thus the lattice parameters for the FeP slab is chosen as the lattice of the heterojunction. Consequently, the $FePO_4$ slab is only slightly compressed upon forming the heterojunction (~2.5%). The heterojunction structure was optimized in two steps. First, an all-atom relaxation of the $FePO_4$ was performed with the frozen FeP slab. Second, the $FePO_4$ and the three atomic layers of FeP close to the interface were relaxed, with the remaining three atomic layers of FeP frozen. The electronic structure analyses for the optimized bulk FeP, bulk $FePO_4$, the heterojunction, and the separate slabs were then performed. Both FeP and $FePO_4$ could exhibit magnetism. Three different spin configurations were considered for the bulk FeP and $FePO_4$, including (1) NS (no-spin), (2) FM (ferromagnetic), and (3) AF (antiferromagnetic).[48] For NS configurations, closed-shell calculations were performed. For FM configurations, unrestricted spin polarization calculations were performed without special spin pre-arrangements. For AF calculations, opposite spins were pre-arranged on different sites of bulk FeP and $FePO_4$. For AF FeP, the opposite spins were assigned with respect to the inversion symmetry. For AF $FePO_4$, a 2×1×1 supercell was used so that the cell contains even number of Fe sites; the opposite spins were assigned to Fe atoms of different primitive cells. For both bulk FeP and $FePO_4$, the AF configuration was predicted to be more thermodynamically favorable than FM and NS. Therefore, the AF spin configuration was selected for the heterojunction system, with the spin pre-arrangement consistent with those for the AF bulk FeP and $FePO_4$.

All of the first-principles calculations were performed using the Vienna Ab Initio Simulation Package (VASP)[49, 50] with the projector-augmented-wave (PAW)[51] potentials. The structure optimization calculations were performed with the pure Perdew–Burke–Ernzerhof (PBE)[52] exchange-correlation functional. Dispersion corrections were included using the

DFT-D3[53] methods. The energy cutoff was set to 500 eV and Monkhorst-Pack grids[54] was used to sample the Brillouin zone (BZ). The 8×8×8, 8×8×8, 2×2, and 2×2 Monkhorst-Pack meshes were adopted for the bulk FeP, bulk $FePO_4$, FeP (010) slab, and $FePO_4$ (010) slab, respectively, and Γ-only calculation was performed for the heterojunction system. For the bulk systems, the equilibrium geometries were fully optimized with both the lattice vectors and atom coordinates relaxed with the tolerance of less than 0.01 eV/Å on each atom. For the slab calculations, a vacuum of 15 Å was used to separate the slab and its periodic images; the lattice vectors are fixed and the atom coordinates are fully relaxed using a convergence criterion of 0.01 eV/Å on each atom.

The single point calculations were carried out for the optimized structures with the hybrid HSE06 functional[55] to generate wavefunctions used in the electronic structure analyses, such as density of states (DOSs) analysis and work-function determination. The total, element-wise, and site-wise DOSs for the investigated systems were predicted at the HSE06 level. Since AF spin configurations, that yield essentially identical DOSs for the α- and β-spin wavefunctions, are thermodynamically favored for the cases, the α- and β-DOSs are summed into the plotted DOSs for better clarity. The work-functions of the slabs were determined as the difference between the vacuum energy and Fermi level energy at the HSE06 level. The Fermi level energy is the band energy for the valence band maximum, and the vacuum energy is determined as the convergence limit for the planar average of the electrostatic potential.

OER free energy profiles were predicted for several surface Fe sites for $FePO_4$ and FeP, also using the above first-principles method.

4. Additional information on Results & Discussion:

A. Optimizing the Pure Phase and Morphology of nano-FeP

The engineering and optimization of nano-FeP were conducted by chemical vapor deposition (CVD) in a quartz tube at 400 °C for 2 h in argon, with varying ratios of precursors as shown in **Table S2**. In the case of the 1:3 ratio, the shape of the nano-particles remained intact during the reaction condition. However, the Fe_2O_3 precursor was not fully converted into FeP due to an insufficient supply of P vapor (**Figure S1**). In the case of the 1:10 ratio, the morphology of the final adducts remained intact but XRD confirmed the presence of Fe_2O_3, FeO and FeP (**Figure S2**). In the cases of 1:40 and 1:60, Fe_2O_3 was fully converted into FeP but the original morphology of nano-particles was lost (**Figures S3-4**). The ratio of 1:20 was the optimal one (**Figures 1c, S6)**.

Table S2 Optimizing the pure phase and morphology of nano-FeP

No.	**wt% of Fe_2O_3:NaH_2PO_2**	**Phase of nano-FeP**	**Morphology**	**Reference**
1	1:3	Not converted (Fe_2O_3)	Intact	**Figure S1**
2	1:10	Mixed Phase (Fe_2O_3, FeP, FeO)	Intact	**Figure S2**
3	1:40	Pure Phase FeP	coalescence	**Figure S3**
4	1:60	Pure Phase FeP	coalescence	**Figure S4**
5	1:20 Optimized ratio	Pure Phase FeP	Intact	**Figure 1c**, **S6**

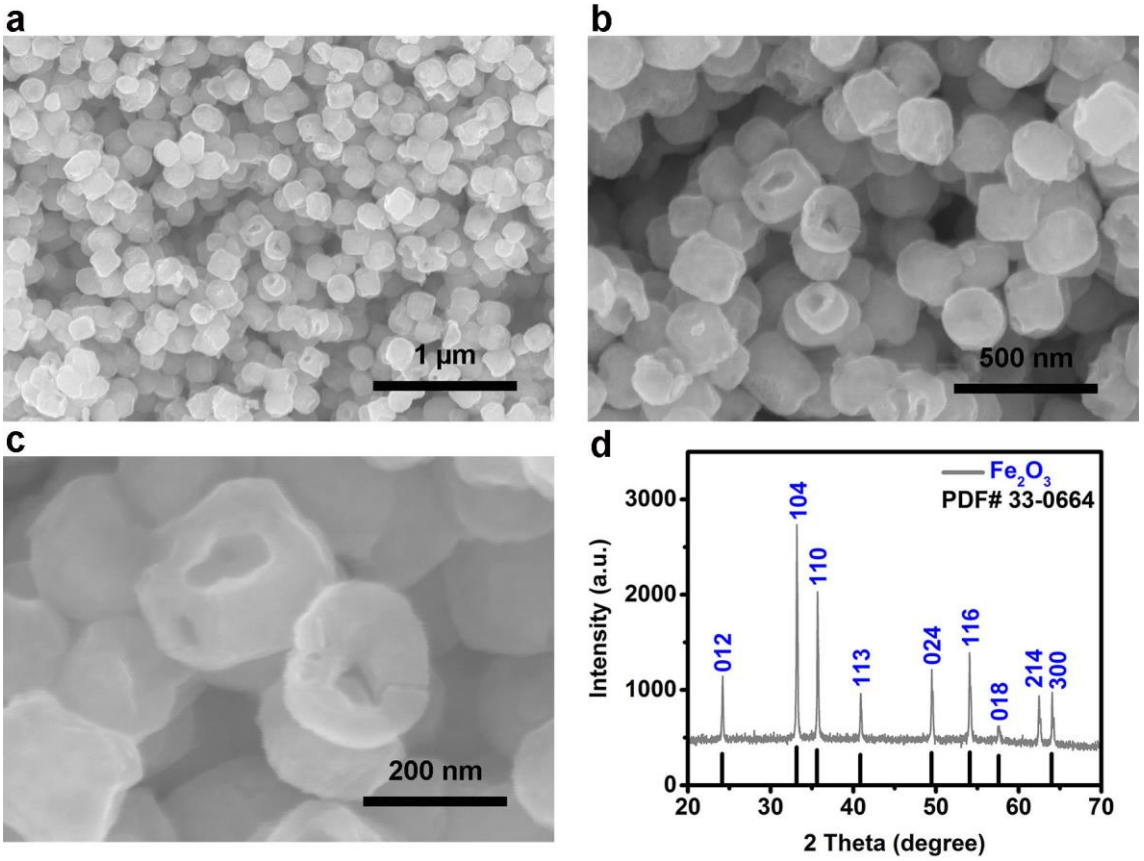

Figure S1 SEM images of the as-prepared product with the wt-ratio of Fe_2O_3: NaH_2PO_2 = 1: 3 at different magnifications with the scale bar of (a) 1 μm, (b) 500 nm, and (c) 200 nm, and (d) XRD patterns of the final product

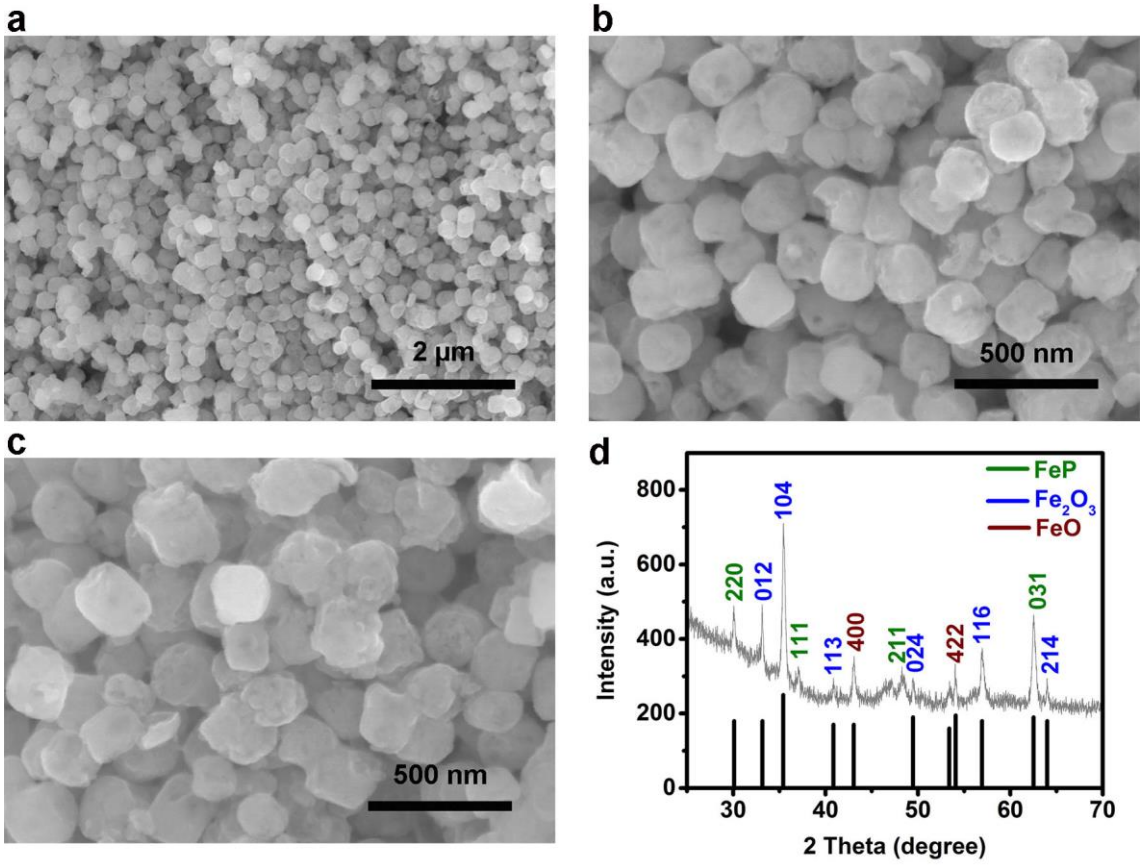

Figure S2 SEM images of the as-prepared product with the wt-ratio of Fe_2O_3: NaH_2PO_2 = 1: 10 at different magnifications with the scale bar of (a) 2 μm, (b) 500 nm, and (c) 500 nm, and (d) XRD patterns of the final product

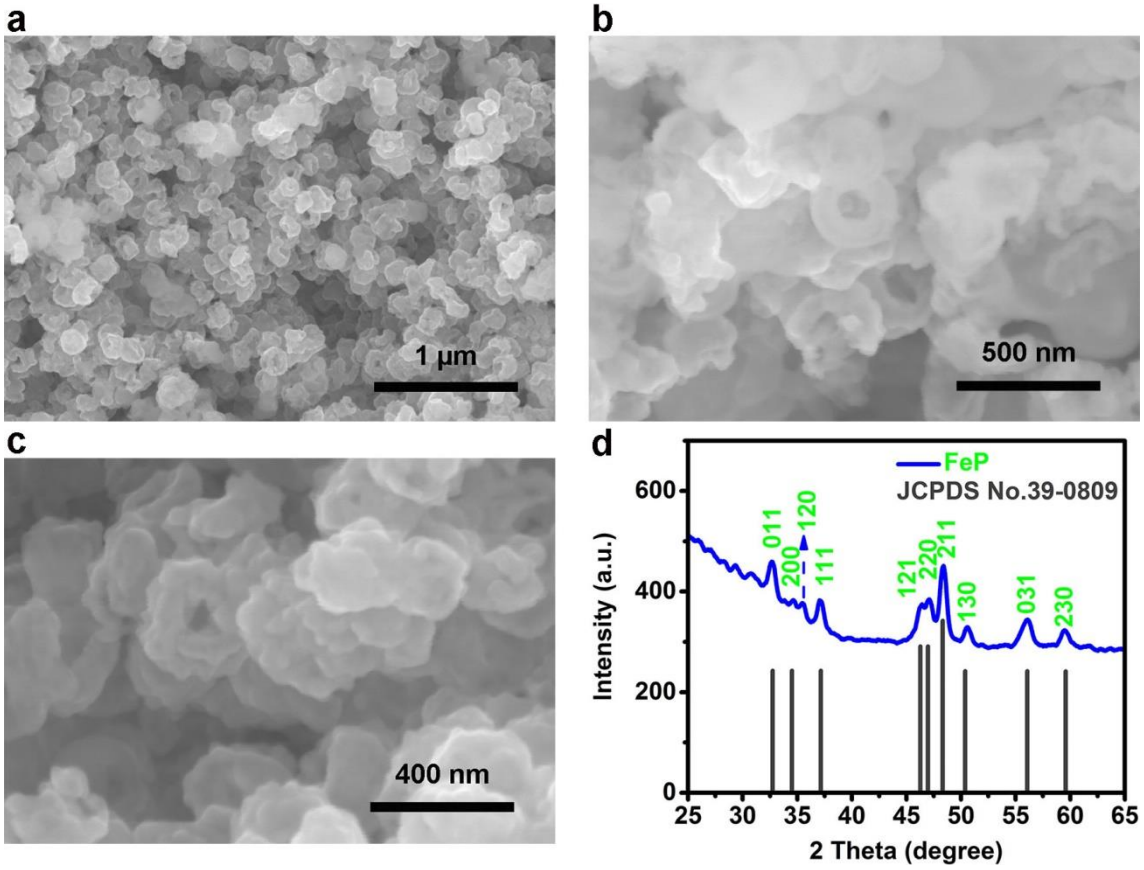

Figure S3 SEM images of the as-prepared nano-FeP nanorings with the wt-ratio of Fe_2O_3: NaH_2PO_2 = 1: 40 at different magnifications with the scale bar of (a) 1 μm, (b) 500 nm, and (c) 400 nm, and (d) XRD patterns of the final product

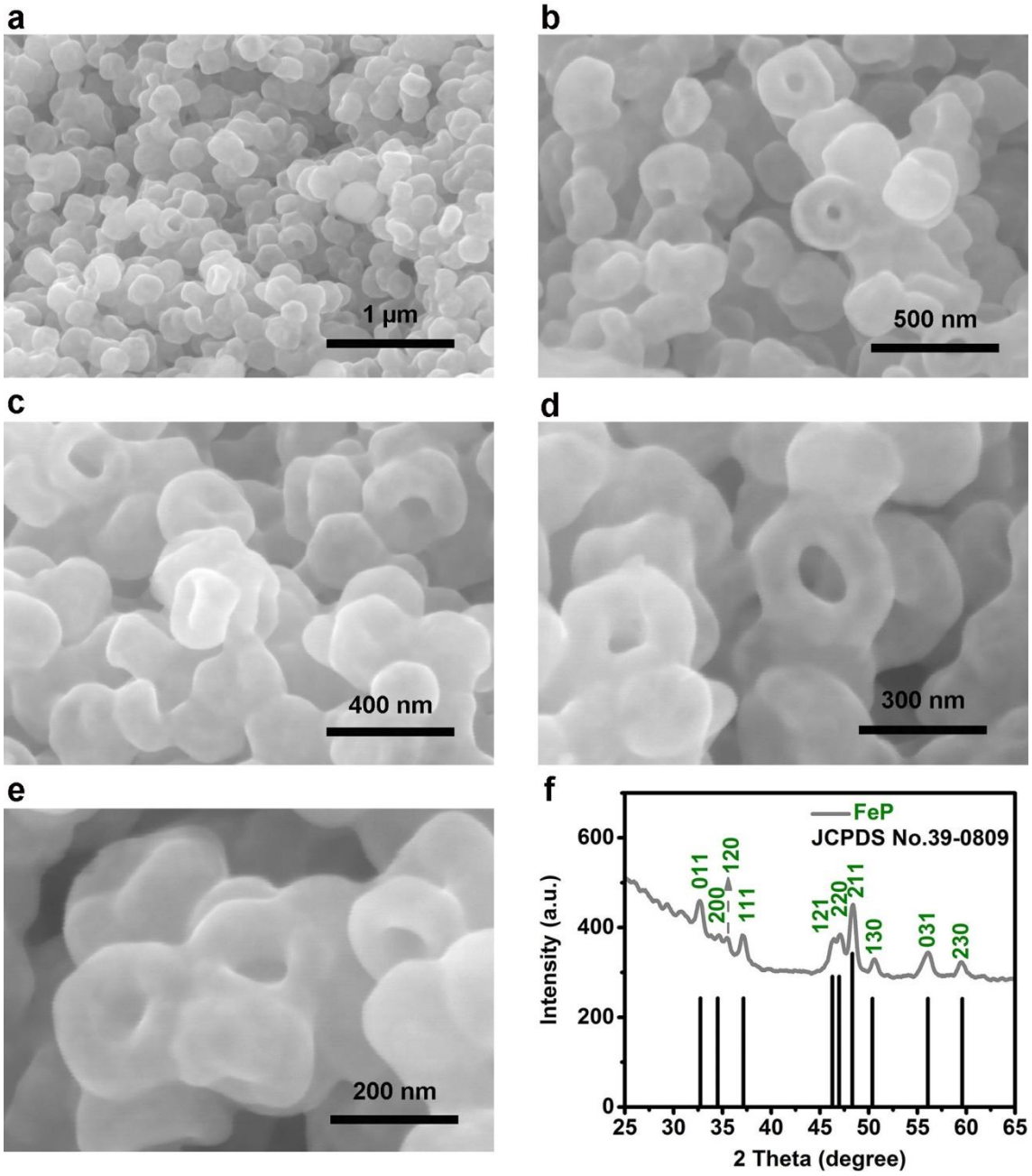

Figure S4 SEM images of the as-prepared nano-FeP nanorings with the wt-ratio of Fe_2O_3: NaH_2PO_2 = 1: 60 at different magnifications with the scale bar of (a) 1 μm, (b) 500 nm, (c) 400 nm, and (d) 300 nm, and (e) 200 nm, and (e) XRD patterns of the final product

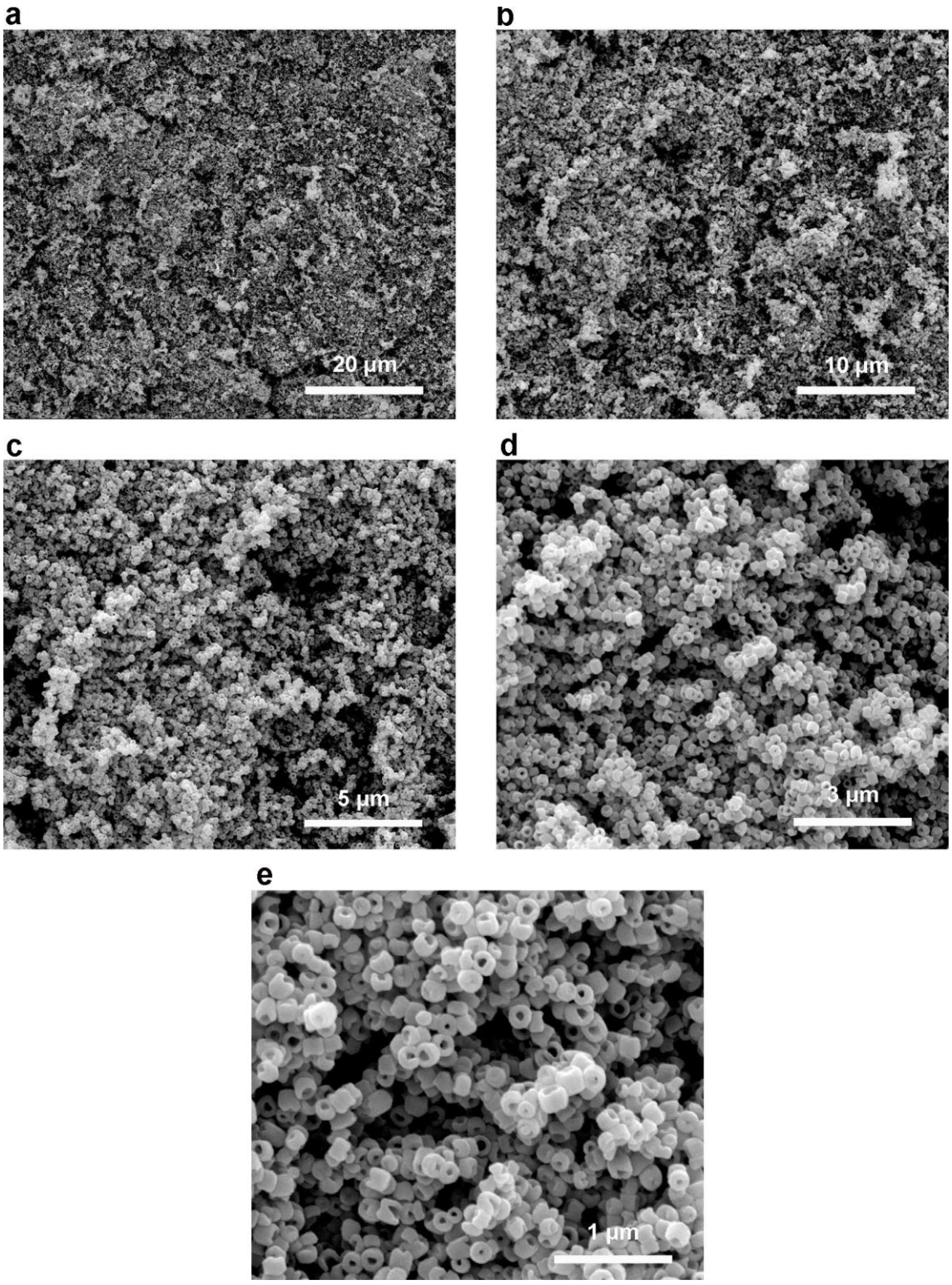

Figure S5 SEM images of Fe_2O_3 nanorings at different magnifications with the scale bar of (a) 20 μm, (b) 10 μm, (c) 5 μm, (d) 3 μm and (e) 1 μm

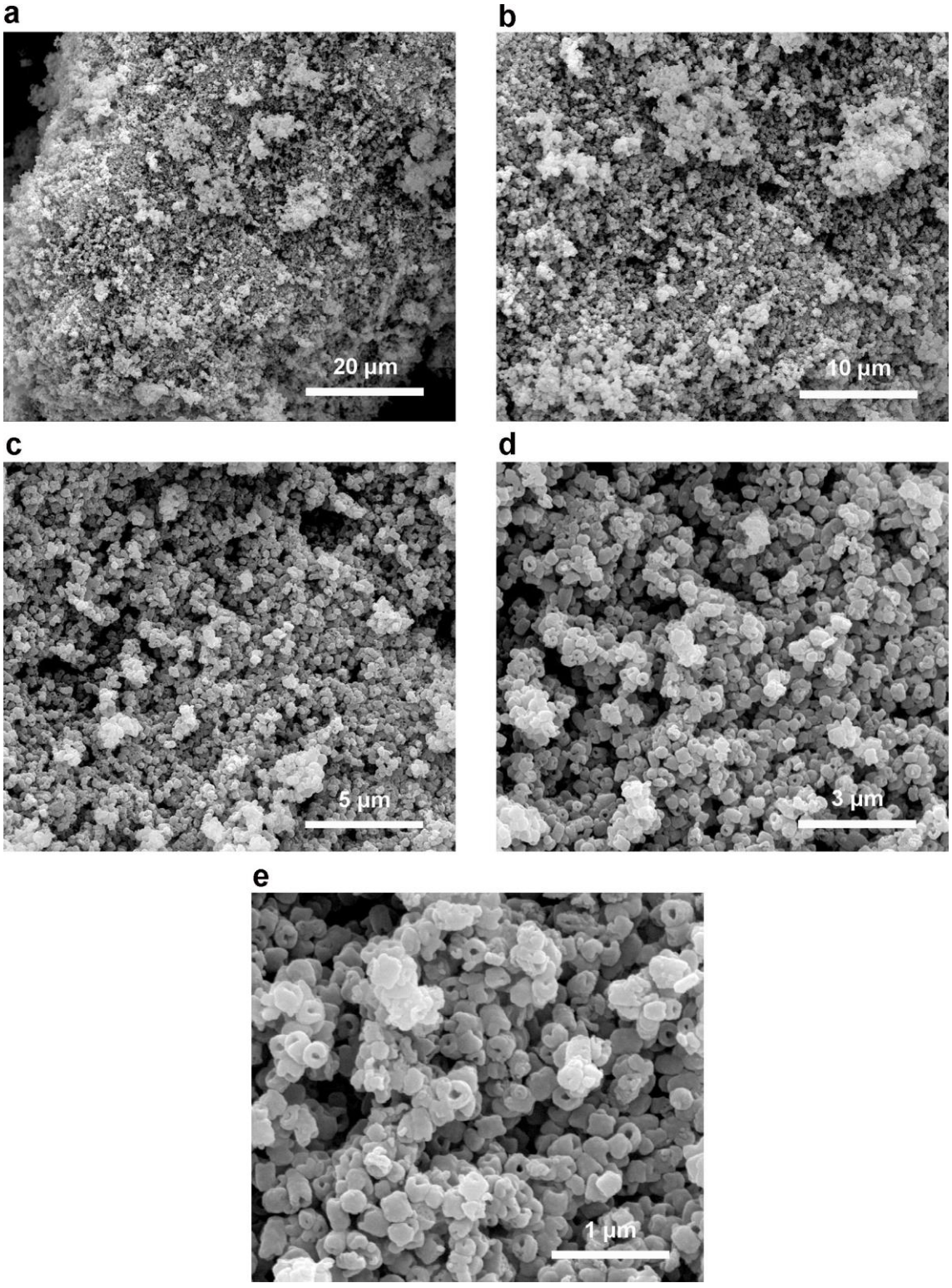

Figure S6 SEM images of nano-FeP at different magnifications with the scale bar of (a) 20 μm, (b) 10 μm, (c) 5 μm, (d) 3 μm and (e) 1 μm

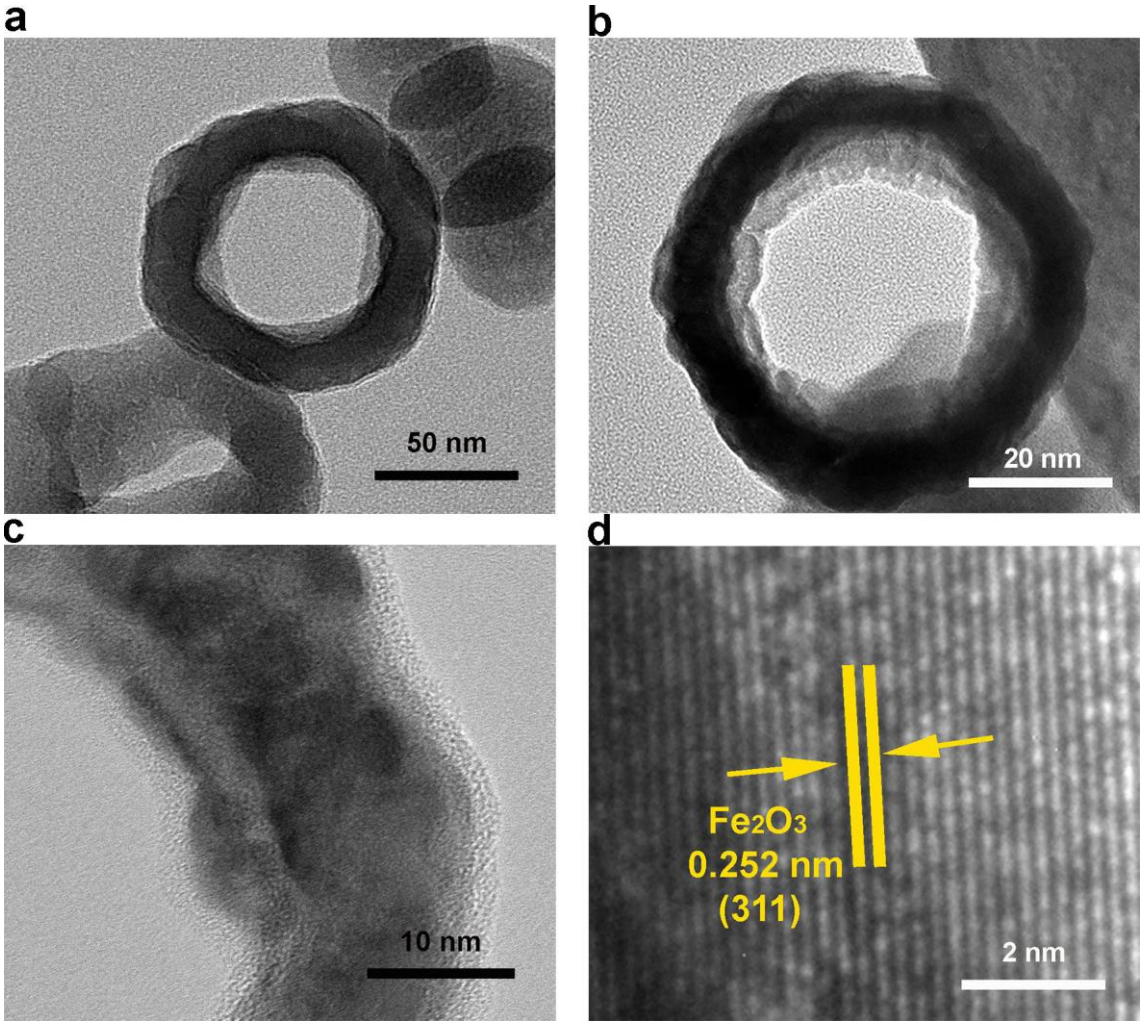

Figure S7 TEM images of the nano-Fe_2O_3 at different magnifications with the scale bar of (a) 50 nm, (b) 20 nm, and (c) 10 nm, and (d) HRTEM image of nano-Fe_2O_3

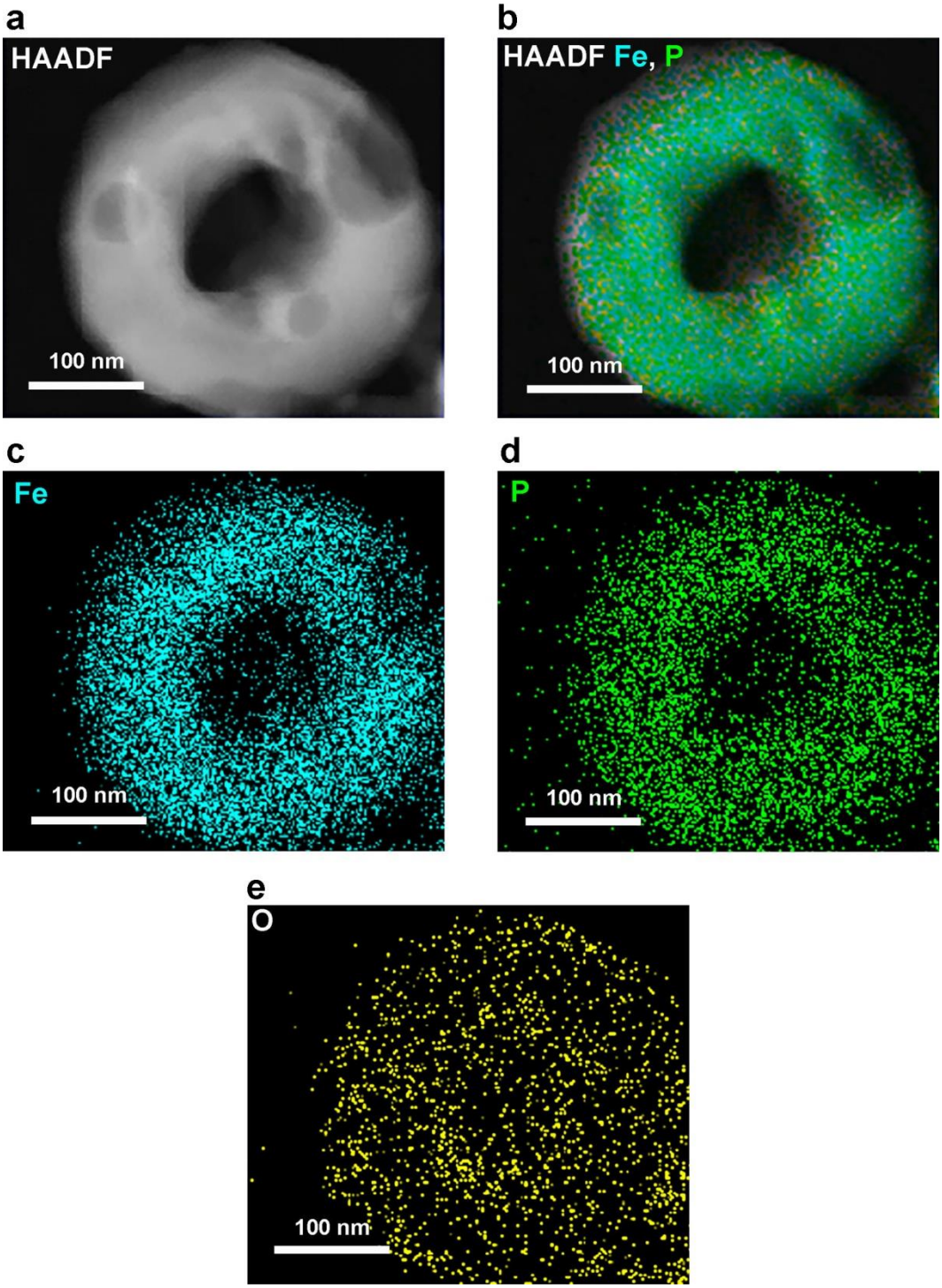

Figure S8 HAADF elemental mapping images of as-synthesized nano-FeP for (a) all elements (b) Fe and P, (c) Fe, (d) P, and (e) O

To further characterize the 3D microstructure of the nano-FeP, we chose two small-areas (Area 1 and Area 2) from the HRTEM image of a nano-FeP sample for FFT analysis. More specifically, Area 1 was selected from the core of the FeP-nanoring and the HRTEM image clearly shows the lattice-fringes and the crystalline nature of FeP in this region. The FFT counterpart shows sharp diffraction spots which can be indexed to (111) and (031). These results are consistent with the XRD results shown in **Figure 1**c of the main text. In comparison, Area 2 was selected from the peripheral of the nanoring and the HRTEM image shows no lattice-fringes in this region. The FFT counterpart shows no diffraction spots and this confirms the peripheral of the FeP-nanoring is amorphous. These results are shown in **Figure S**9. The average thickness of this amorphous "shell" is about 5 nm. As shown in **Figure 2** in the main text, XPS suggests that the composition of this amorphous "shell" is $FePO_4$.

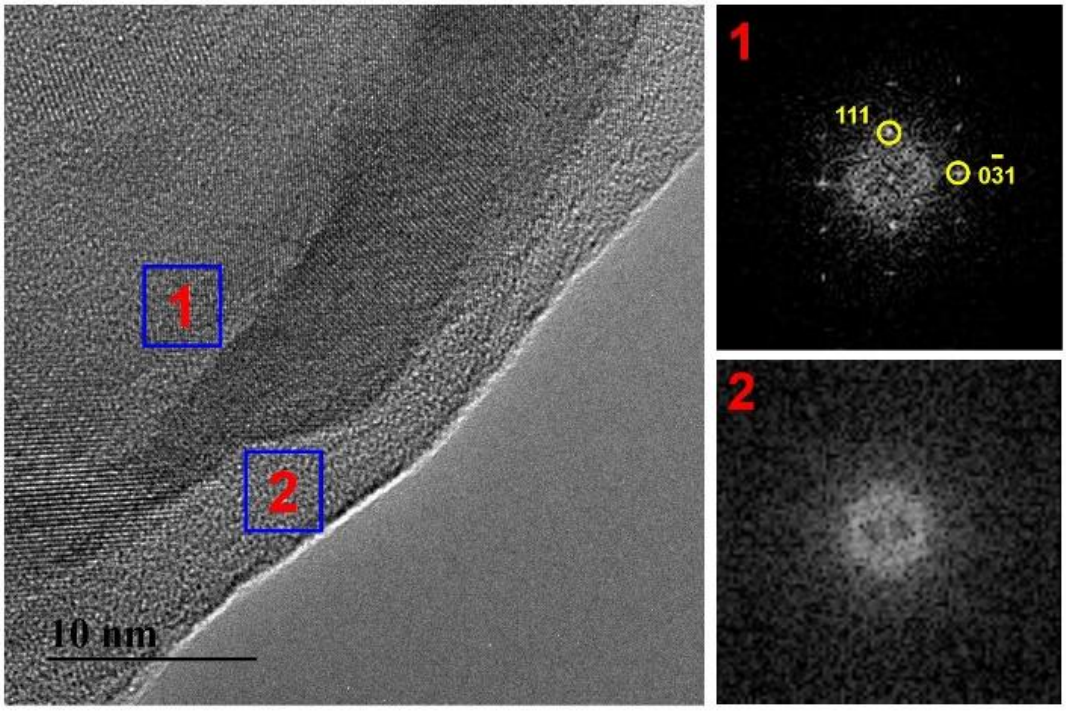

Figure S9 HRTEM lattice-imaging and small-area diffraction analyses of FeP (Area 1) and $FePO_4$ (Area 2)

B. Additional Information on Surface and Materials Characterization

The process engineering and optimization leading to the nano-FeP yielding the lowest cell-voltage and highest operation-stability are detailed in the preceding section, particularly in **Table S2** and **Figures S1-4**. A comparison of the XRD analysis of the nano-Fe_2O_3 prior to phosphidation and that of the resultant nano-FeP, as shown in **Figure 1c**, clearly confirms the complete conversion of the α-Fe_2O_3 precursor (JCPDS No. 33-0664) to orthorhombic-FeP (JCPDS No. 39-0809). The nano-FeP morphology is engineered, with the nano-ring morphology of nano-Fe_2O_3 shown in **Figure S5** as a template, to a nano-ring-like shape as shown by the SEM and TEM images (**Figure 1d and Figure S6)**. Each nano-ring actually comprises nano-FeP grains packed into a porous structure as shown by the TEM image in the inset of **Figure 1d**. The lattice of a typical nano-grain locating at the outer-rim of an nrFeP is shown in **Figure 1e** and the lattice can be indexed to that of FeP. This particular lattice image also reveals the presence of an amorphous overlayer with a thickness of ~5 nm. The composition of this overlayer is revealed by XPS to be $FePO_4$ grown on FeP due to natural surface oxidation (**Figure 2)**. In short, a cell is constructed, as shown in **Figure 1b**, with a heterojunction bifunctional catalyst derived from natural surface oxidation of nano-FeP, i.e., $FePO_4$/FeP. Remarkable, this simple cell splits water with a low cell-voltage of 1.40 V (at 10 mA/cm^2) which pushes the recent trend of cell-voltage reduction a little closer to the thermodynamic limit of 1.23 V, as shown by the comparitive chart in **Figure 1e**. An extension of this comparitive analysis is included in **Table S1**.

The formation of a $FePO_4$/FeP heterojunction structure *via* natural surface oxidation of FeP is vividly evident from XPS. Firstly and most importantly, the Fe 2p (**Figure 2a**) and P 2p (**Figure 2b**) XPS spectra unambiguously show both $FePO_4$ (Fe $2p_{3/2}$ at ~711 eV and P 2p at ~134 eV) and FeP (Fe $2p_{3/2}$ at ~707 eV and P 2p at ~129 eV), when an electrode loaded

with nano-FeP is inspected by XPS. The spectral assignments are consistent with those made and cited by Yu, et al.[2] With the hypothesis of an overlayer of $FePO_4$ on FeP, which is supported by the HRTEM result in **Figure 1e**, the overlayer thickness can be computationally deduced from the phosphate/phosphide XPS-spectral ratio in **Figure 2b**. Basically, the thickness of an overlayer is equal to λln{[calibrated XPS signals of the overlayer]/[calibrated XPS signals of the underlayer]+1}when XPS signals are collected along the normal direction of a bilayer sample. In the case of phosphate/phosphide, λ is the photoelectron inelastic mean-free-path of p 2p and is about 3nm. The calculated phosphate overlayer-thickness value is ~5 ±1 nm which agrees well with the HRTEM result (**Figure 1e**). In addition, the XPS Fe, P, and O signals, when calibrated with their atomic XPS cross-sections, further nail the compositional identification of such a heterojunction with ~5 nm of $FePO_4$ on FeP.

More importantly, XPS analysis of this $FePO_4$/FeP heterojunction further reveals insightful electronic structures for the clarification of how $FePO_4$/FeP works as an effective bifunctional catalyst for water-electrolysis. Specifically, a comparison of the XPS valence band spectra of a gold reference and the $FePO_4$/FeP electrode-sample, as shown in **Figure 2c**, reveals that the VBM of the $FePO_4$ overlayer is located at 1.3 ± 0.1 eV from the Fermi level (i.e., $E_{VBM,\ FePO4} - E_{FL} = 1.3 \pm 0.1$ eV). This measurement method adopts the photoemission of gold starting at its Fermi level, which aligns with the Fermi level of the spectrometer, as an internal reference. The binding-energy of the onset of the gold photoemission is not at 0.0 eV but at -1.3 eV because the experimental spectral resolution of the spectrometer inevitably spreads and extends the onset of the gold photemission to a peculiar negative binding-energy value. With this gold onset to define the location of Fermi level for any test-sample properly grounded in the spectrometer, a measurement of the photoemission onset of an unknown semiconducting sample, *i.e.*, VBM of a semiconductor, under the exact spectrometer-operation conditions for measuring the gold onset, gives the seperation between the VBM and Fermi level of the unknown sample. With this method, the photoemission onset of the $FePO_4$

overlayer is found at 0.0 eV; therefore, the VBM location of the $FePO_4$ overlayer is at 1.3 ± 0.1 eV from its Fermi level. This finding is an important piece of information regarding the working mechanism of the $FePO_4$ semiconductor-overalyer as a bifunctional catalyst.

The surface area and porous structure were further characterized by N_2 adsorption/desorption measurements. The transformation from oxide to phosphide led to an increase in density and a slight decrease in the total surface area. The pore size slightly decreased after phosphidation of Fe_2O_3 due to the growth of FeP crystallites. Moreover, a slight rearrangement in porosity was also observed where new pores of ~10 nm were found (**Figure S10**).

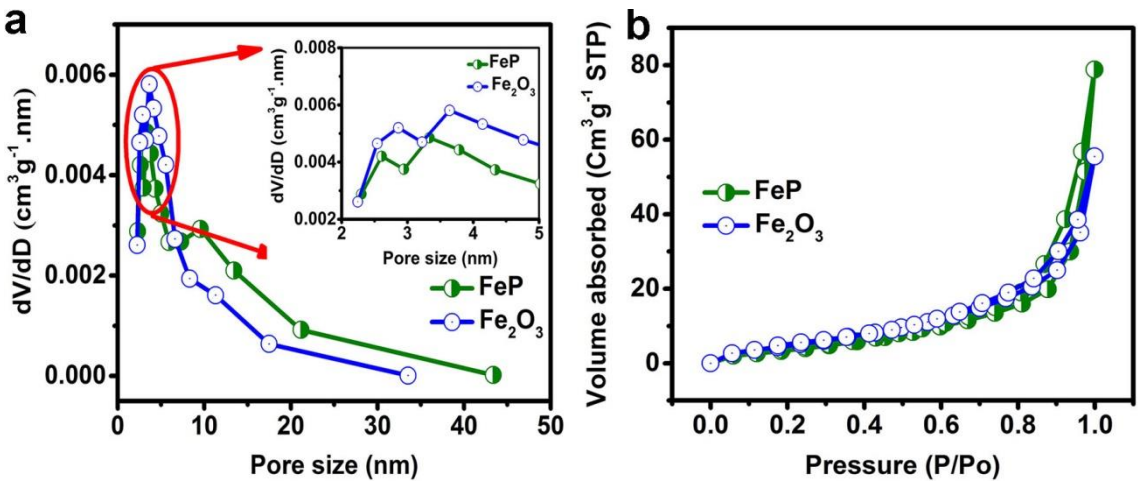

Figure S10 (a) Pore size distribution curves for as-synthesized nano-FeP and nano-Fe_2O_3 and (b) the corresponding N_2 adsorption–desorption isotherms using the BJH method

C. Additional Results on Electrochemistry

(1) Electrochemical impedance spectroscopy

a. Comparison of the impedance of nano-FeP and nano-Fe_2O_3

A set of comparative electrochemical impedance spectra (EIS) are shown in **Figure S11**, for the illustration of the electrochemical differences between catalysts derived from nano-FeP and nano-Fe_2O_3. In brief, the impedances of the electrodes loaded with nano-FeP (actually $FePO_4$/FeP) are lower than those of the electrodes loaded with nano-Fe_2O_3. The equivalent capacitance of the electodes loaded with nano-FeP in the cell-operation are higher than those with nano-Fe_2O_3.

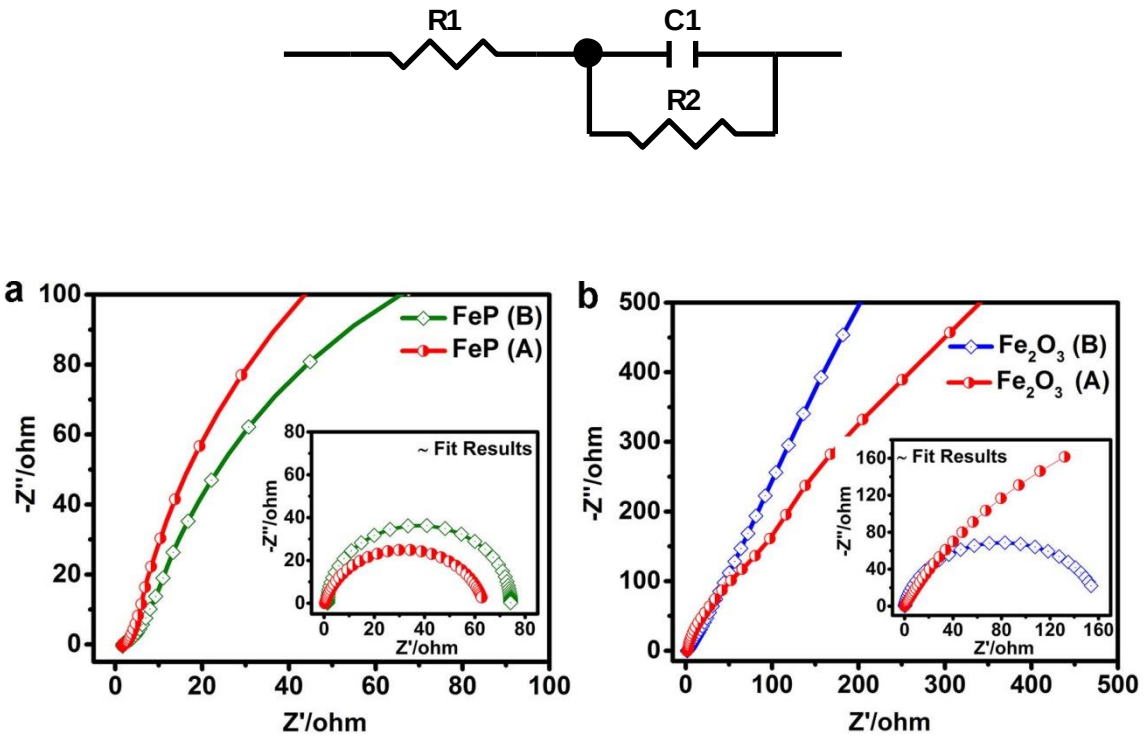

Figure S11 Nyquist curves derived from EIS measurements for (a) nano-FeP and (b) nano-Fe_2O_3. "B" and "A" indicate before and after the LSV test, respectively

(b) Flatband measurements on $FePO_4$/FeP

EIS was used to extract the capacitance of an electrode loaded the $FePO_4$/FeP catalyst, and the Mott–Schottky plots (**Figures S12a and S12b**) were constructed to probe the density of states near CBM (**Figure S12**a) and near VBM (**Figure S12b**). The measurements were made in 1M KOH at 1000 KHz in a three-electrode-configuration. The Mott-Schottky plot probing the conduction band reveals that the conduction band of $FePO_4$ comprises a first weak and narrow DOS band and, deeper into the conduction band, a second strong and broad DOS band. As such, $1/C^2$ becomes small but yet not close to zero when the first weak and narrow DOS band is probed. When the second DOS band is probed, $1/C^2$ drops and eventually becomes close to zero. This peculiar band structure is confirmed by our DFT computation (**Figure 4** and **Figures S23b**)

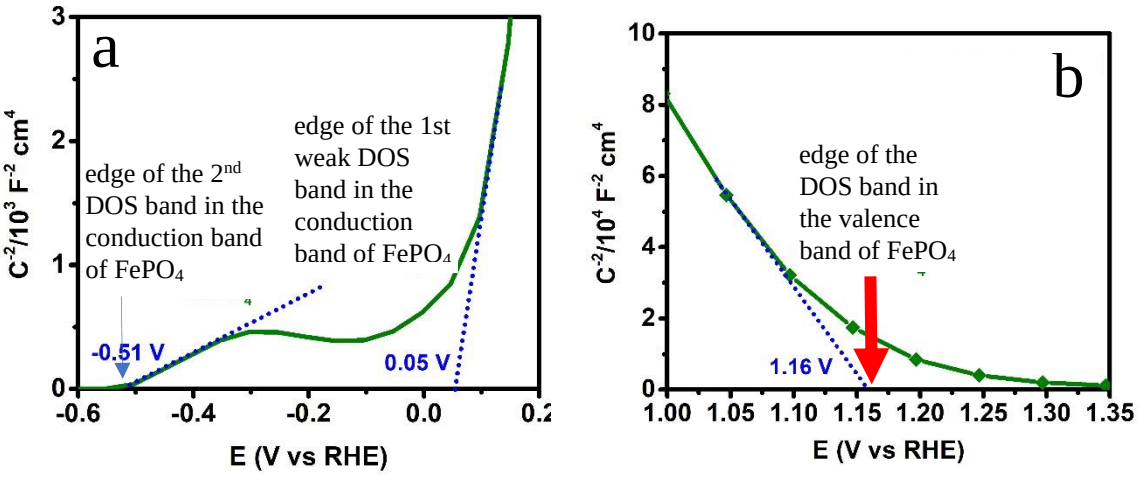

Figure S12 Mott–Schottky plots for $FePO_4$/FeP for (a) probing CBM and (b) probing VBM.

(2) More results on HER in 1 M KOH

HER measurements were carried out in a 3-electrode-configuration in 1 M KOH. In addition to the HER data in **Figure 3a, Figure S13a** shows an enlarged linear-sweep-voltammetry (LSV) plot for further clarifying the low-overpotential performance. **Figure S13b** compares the Tafel slopes of $FePO_4$/FeP, Fe_2O_3, and Pt/C. Evidently, $FePO_4$/FeP is comparable to Pt/C and is much better than Fe_2O_3. Moreover, **Figure S13c** shows that $FePO_4$/FeP exhibits an electrochemical double-layer capacitance (C_{dl}) of 85.3 mF/cm^2 which is much larger than that of Fe_2O_3 (12.1 mF/cm^2). In addition, the durability of $FePO_4$/FeP is illustrated in **Figures S13d** which demonstrates little loss in activity and current density in an operation-duraction of 50 h. The evolution of hydrogen was also tracked in this test and the results are included in **Figures S13d**. Further, LSV plots taken before and after the 50h-durability-test are compared in **Figures S13e** to demonstrate that the change in overpotential is small.

Figure S14 compares the HER performance of the present work with the prior-art exemplars.

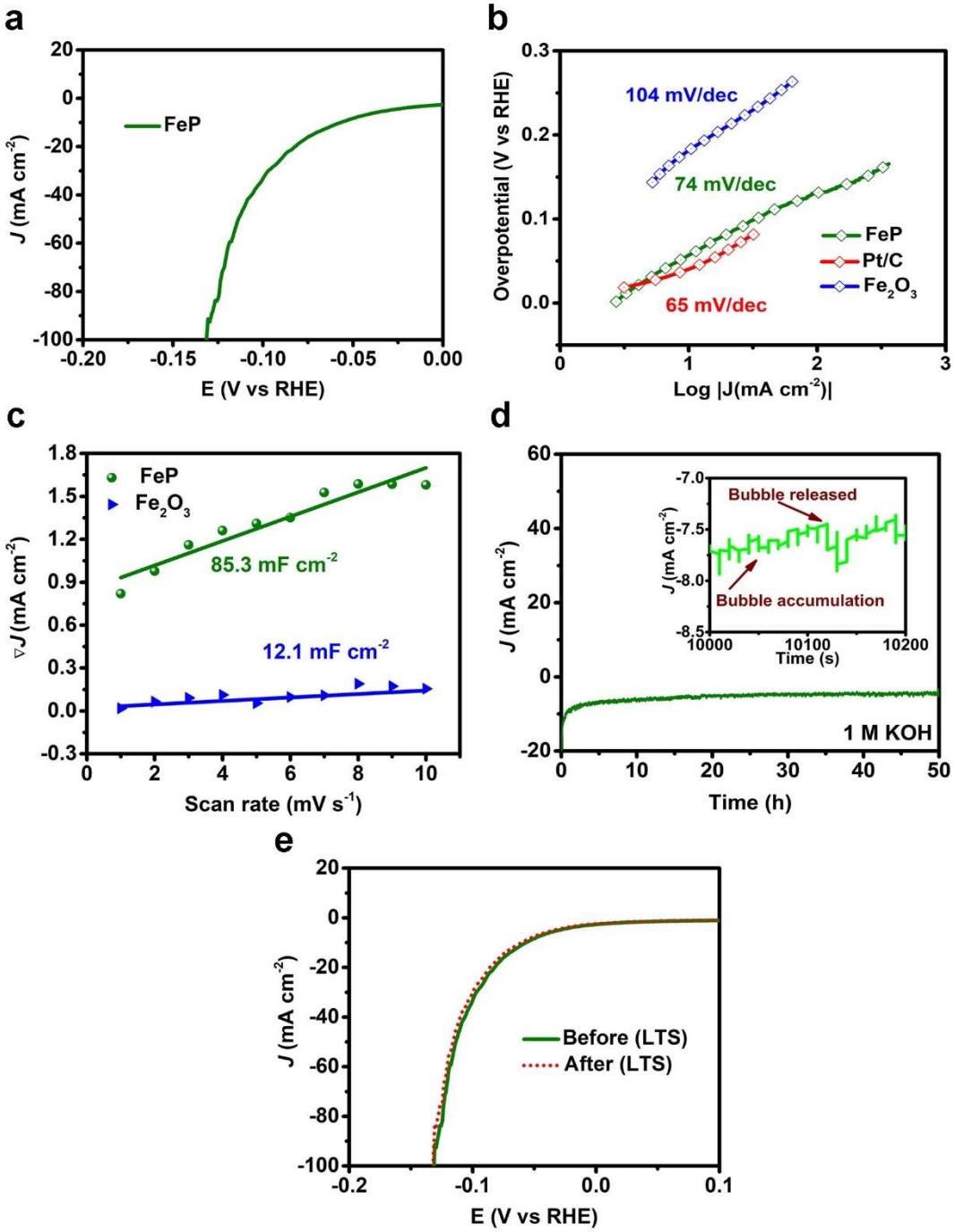

Figure S13 (a) HER performance of nano-FeP, (b) HER Tafel slopes for nano-FeP, Pt/C and nano-Fe_2O_3, (c) current density differences (at a potential of 0.1 V vs RHE in 1 M KOH) plotted against the scan rate with fitted electrochemical surface area (ECSA) slopes, (d) amperometric i-t responses of nano-FeP at -1.052 V vs Ag/AgCl for 50 h (inset: the enlargement of the long term stability curve from 10000 to 10200 s), and (e) polarization curves of nano-FeP taken before and after the stability testing for 50 h during HER. All the measurements are taken at room temperature, FeP means nickel foam loaded with nano-FeP

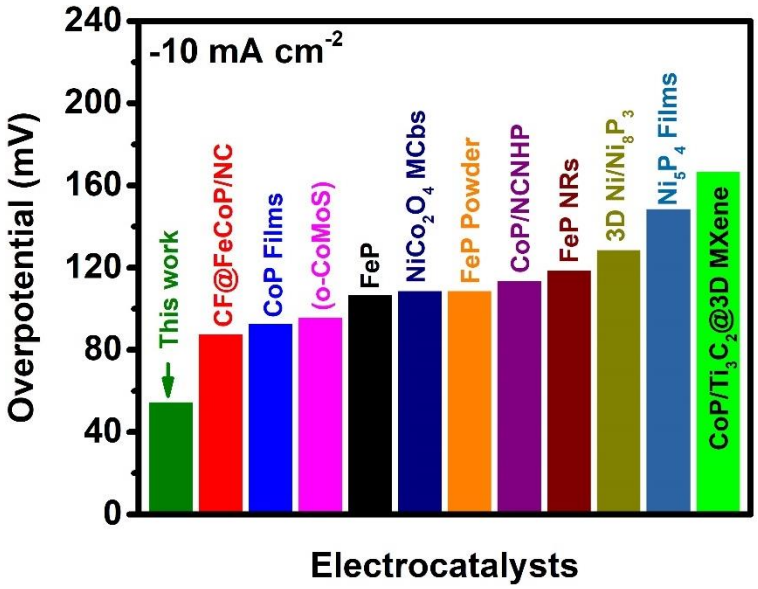

Figure S14 A comparitive analysis of electrochemical performances of different electrocatalysts for HER at a curent density of 10 mA/cm^2 with a nickel-foam anode loaded with nano-FeP

(3) More results on OER in 1 M KOH

In addition to the OER data in **Figure 3b**, **Figure S15a** shows an enlarged linear-sweep-voltammetry (LSV) plot for further clarifying the low-overpotential performance. **Figure S15b** compares the Tafel slopes of $FePO_4$/FeP, Fe_2O_3, and Pt/C. Evidently, $FePO_4$/FeP (27 mV/dec) is much better than Fe_2O_3 (150 mV/dec) and RuO_2 (104 mV/dec). Moreover, **Figure S15c** shows that FePO4/FeP exhibits an electrochemical double-layer capacitance of (C_{dl}) 11.2 mF/cm^2 which is larger than that of Fe_2O_3 (5.0 mF/cm^2). In addition, the durability of $FePO_4$/FeP is illustrated in **Figures S15d** which demonstrates little loss in activity and current density in an operation-duraction of 50 hours. Further, LSV plots taken before and after the 50h-durability-test are compared in **Figures S15e** to demonstrate that the change in overpotential is small.

Figure S16 compares the OER performance of the present work with the prior-art exemplars.

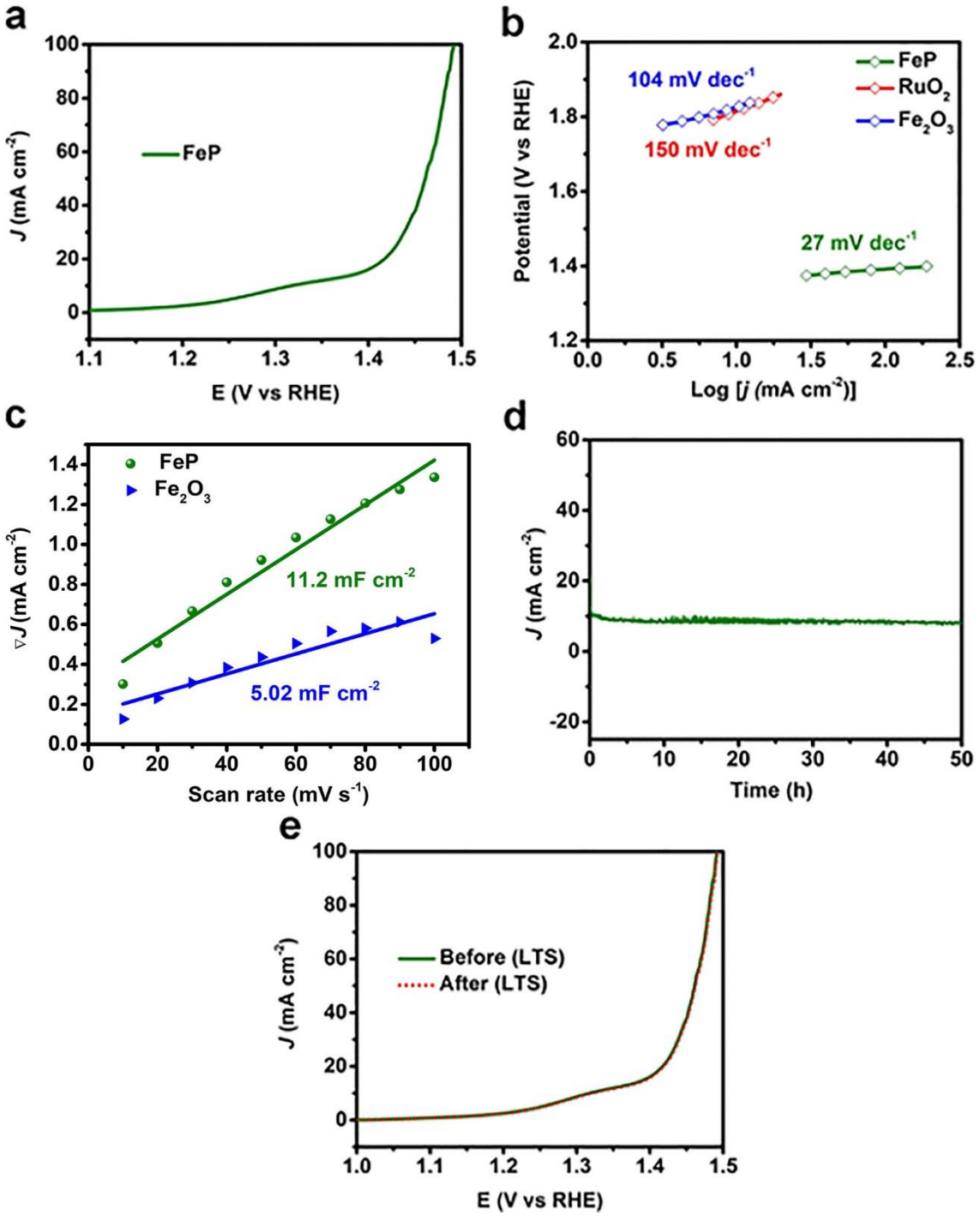

Figure S15 (a) OER performance of nano-FeP, (b) OER Tafel slopes of nano-FeP, RuO_2 and nano-Fe_2O_3, (c) current density differences (at a potential of 1.08 V vs RHE in 1 M KOH) plotted against the scan rate with fitted ECSA slopes, and (d) amperometric i-t responses of nano-FeP at 0.32 V vs Ag/AgCl for 50 h during OER and (e) the polarization curves of nano-FeP taken before and after the stability test for 50 h for OER.

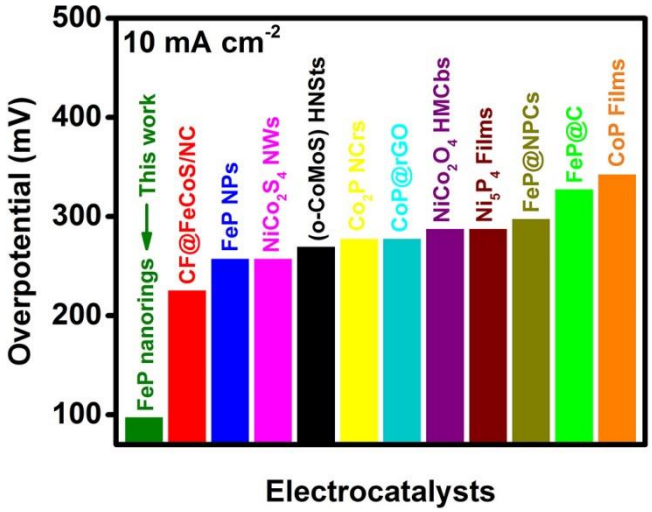

Figure S16 A comparitive analysis of electrochemical performances of different electrocatalysts for OER at curent density of 10 mA/cm^2 with a nickel-foam anode loaded with nano-FeP

(4) Full-cell reactions

Figure S17a shows the LSV curve of the full-cell with its current desnity rising up to 50 mA/cm^2. **Figure S17b** compares the Tafel slopes for nano-FeP//nano-FeP, Pt/C//RuO_2 and Fe_2O_3//Fe_2O_3, and the respective values are 125, 185 and 209 mV/dec. Obviously, the full-cell with nano-FeP is more practical than its peers in this comparison. Furthermore, the durability of the FeP//FeP system is reasonably good, as shown in **Figures S17c-d**

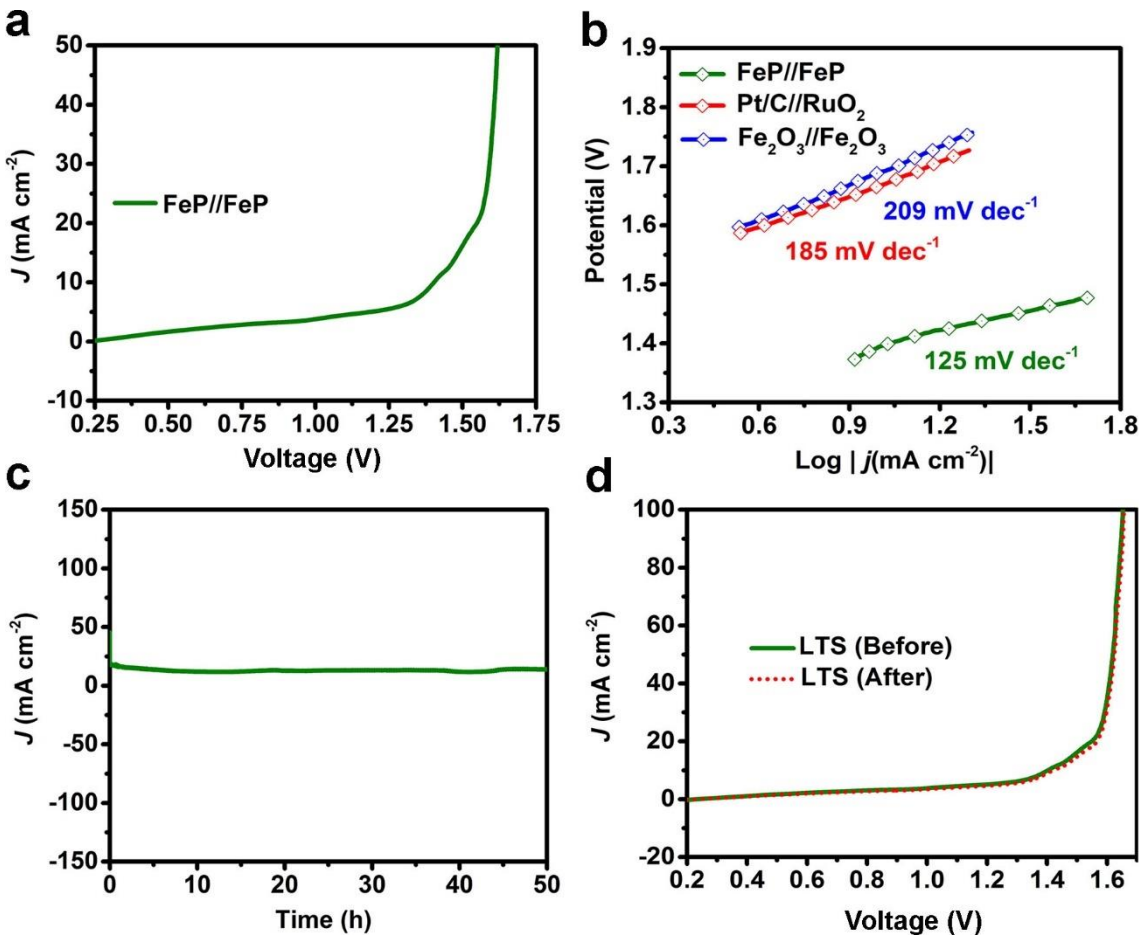

Figure S17 (a) Full-cell performance of nano-FeP, (b) Tafel slopes of the full-cells including nano-FeP//nano-FeP, Pt/C//RuO_2 and nano-Fe_2O_3//nano-Fe_2O_3, (c) amperometric i-t responses of nano-FeP//FeP cells at a constant voltage of 1.51 V for 50 h with a starting current density of 20 mA/cm^2, and (d) the polarization curves recorded before and after the stability test

(5) Faradaic efficiency

Faradaic efficiency was tracked during a full-cell operation (1.57 V and 100 mA/cm^2) by collecting the emitted hydrogen and oxygen. $FePO_4$/FeP exhibited an average efficiency of 99% for an operation-span of 50 min. The measurements are sumarized in **Figures S18a-d**.

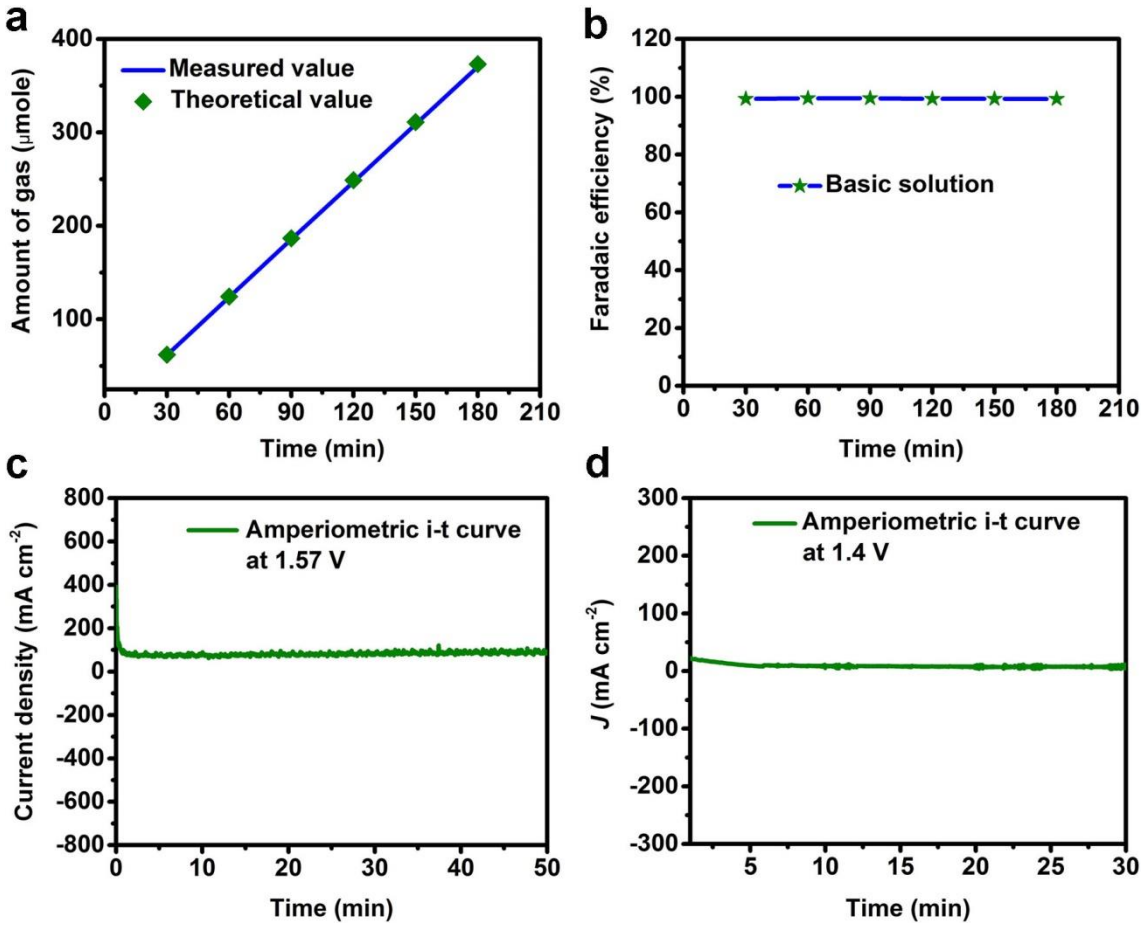

Figure S18 (a) The measured and theoretical gas-emission from $FePO_4$/FeP at 1.57 V, (b) plot of Faradaic efficiency (%) at different time intervals, and (c) the amperometric i-t curve recorded at the current density of 100 mA/cm^2, and (d) the amperometric i-t curve recorded at the current density of 10 mA/cm^2. The readings were recorded at room temperature (26 °C), 1 atmospheric pressure and in 1 M KOH solution.

(6) Electrochemical-Surface-Area measurements

Cyclic voltammograms (CV) in scan rates ranging from 1 to 10 mV/s and 10 to 100 mV/s for HER and OER, respectively, are included in **Figures S19** and **S20**. These data were used to estimate capacitance-results and other relevant results in this work.

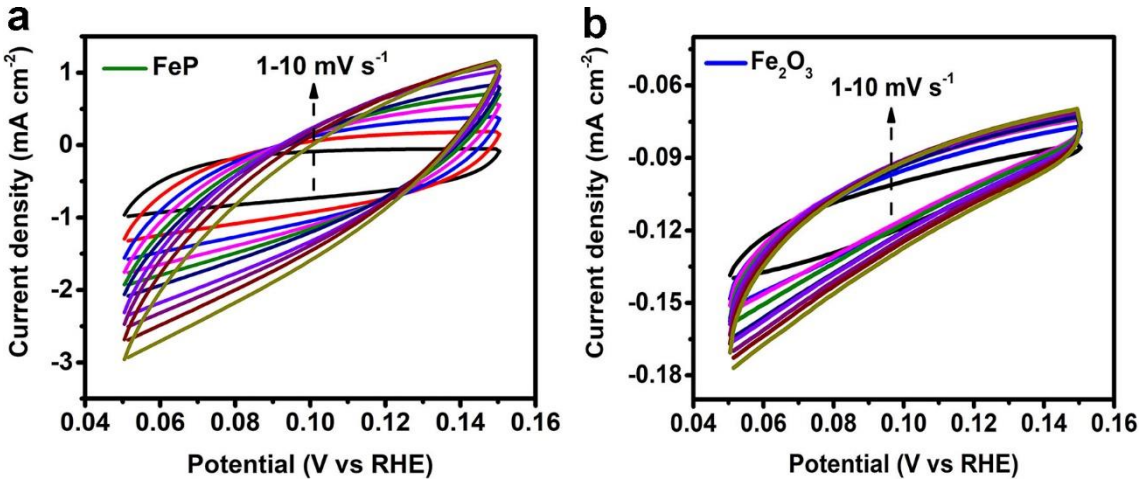

Figure S19 Cyclic voltammograms (CV) for (a) nano-FeP in the voltage range of 0.05~0.15 V vs RHE and (b) nano-Fe_2O_3 in the range of 0.05~0.15 V vs RHE in 1 M KOH, with scan rates ranging from 1 to 10 mV/s

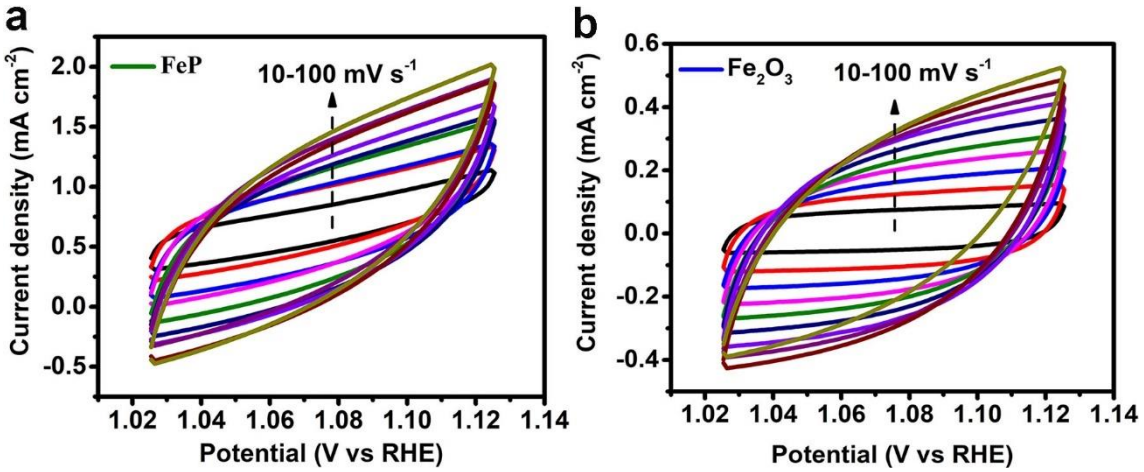

Figure S20 Cyclic voltammograms (CV) for (a) nano-FeP in the voltage range of 1.025 ~ 1.125 V vs RHE and (b) nano-Fe_2O_3 in the range of 1.025 ~ 1.125 V vs RHE in 1 M KOH, with scan rates ranging from 10 to 100 mV/s

D. HRTEM of $FePO_4$/FeP after a 24h-stability-test for HER and OER

After a stability test of HER for 24 h, HRTEM was applied to the tested $FePO_4$/FeP- cathode. The presence of a crystalline FeP core and an amorphous shell were evident (**Figure S21**a). The observed lattice spacing of 0.190 nm can be indexed to the (012) lattice planes of FeP, and this proves the retention of FeP. The presence of an amorphous shell of about 5nm suggests that the 24h-HER-test did not etch the amorphous oxidized shell present prior to the 24h-HER-test. Apparently, the generation of atomic hydrogen on the cathode-surface during HER is not sufficient to reduce and remove the oxidized species on FeP. The reduction of iron oxide and iron phosphate probably require atomic hydrogen at a high temperature.

Similarly, HRTEM of the OER-anode after a 24h-stability-test also revealed the presence of lattice-fringes belonging to FeP in the core of the nano-particles on the OER-anode and the presence of an amorphous shell. **Figure S21b** shows the lattice-fringes of FeP (131) lattice planes of FeP. The average thickness of the amorphous shell increased to about 10nm as a result of OER for 24 h. Apparently, the oxidants leading to the evolution of O_2 on the anode surface is strong enough to cause the observed increase of oxidation-depth into the core of FeP.

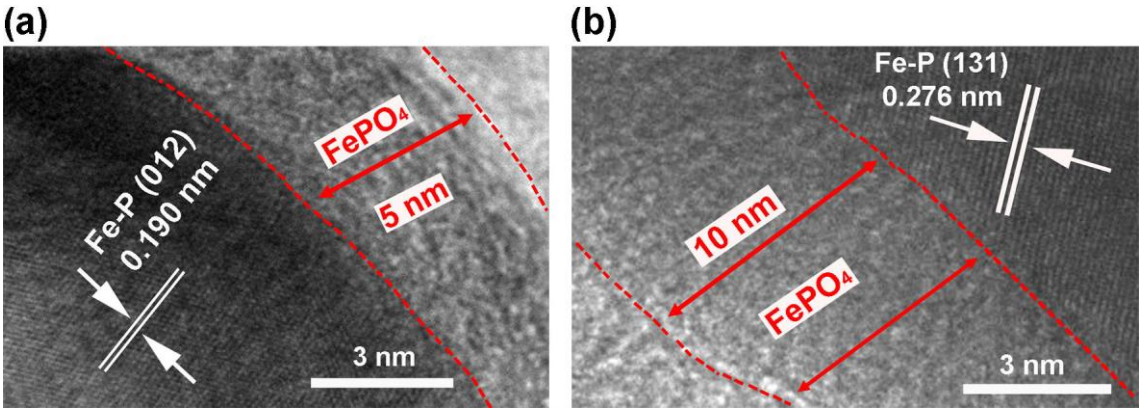

Figure S21 HRTEM images of $FePO_4$/FeP after a 24h-stability-test (a) $FePO_4$/FeP on the HER-cathode and (b) $FePO_4$/FeP on the OER-anode

E. Results on Work-function Measurements

A comparison of the UPS valence band spectra of gold and the FeP/$FePO_4$ electrode-sample, reveals an ex-situ work-function of 5.1 ± 0.1 eV for polycrystalline gold and 4.7 ± 0.1 eV for the $FePO_4$/FeP sample, as shown in **Figure S22**. The result on gold is typical, and that on $FePO_4$/FeP is new. In this context, ex-situ work-function means the energy separation from the Fermi level of the electrode-sample to the referencing vacuum-energy-level, when the sample is taken out from the electrolysis-cell and placed in ultrahigh vacuum. In this work, in-situ work-function measurements were probed by Mott-Schottky analysis.

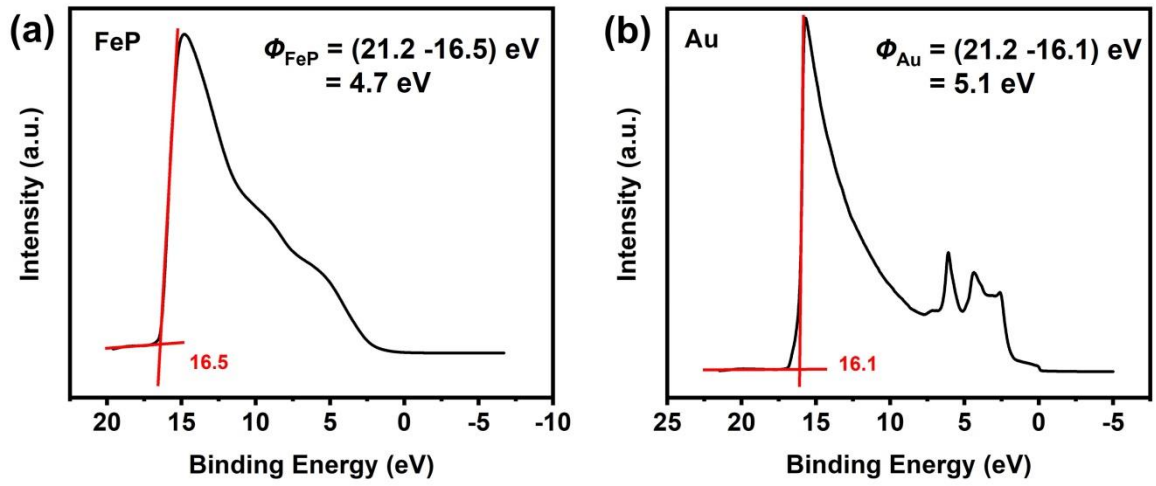

Figure S22 UPS test to get the work-function of (a) $FePO_4$/FeP =4.7 ±0.1 eV and (b) Au = 5.1±0.1 eV

F. Determination of VBM and CBM of $FePO_4$ in FeP/$FePO_4$ Heterojunction

The energy positions of the VBM and CBM for the $FePO_4$ overlayer of FeP/$FePO_4$ heterojunction are determined on the basis of the comparative analysis of the element-wise PDOSs for the bulk $FePO_4$ and the overlayer $FePO_4$ in the heterojunction. The element-wise PDOS for the bulk $FePO_4$ **Figure S23a** clearly indicates that the VBM is contributed comparably both O- and Fe- PDOSs (Fe:O ≈ 1:1), whereas the CBM is dominated by Fe-

PDOS (Fe:O ≈ 2:1). The corresponding CBM and VBM bands can hence be determined based on the Fe:O PDOS ratio for $FePO_4$ in $FePO_4$/FeP. The bands with VBM-character are found in the range of -2.5 to -1.0 eV, w.r.t. the Fermi level, and the bands with CBM-character are found in the range of -1.0 to 0.5 eV. The splitting of CBM and VBM bands are due to the different chemical environments of $FePO_4$ layers as illustrated in **Figure 4d**. It is also noted that in the energy range of -1.5 to 0.1 eV, many surface states and interface states are present and critically affect the bandgap properties and thereby electrochemical properties of $FePO_4$ in the heterojunction.

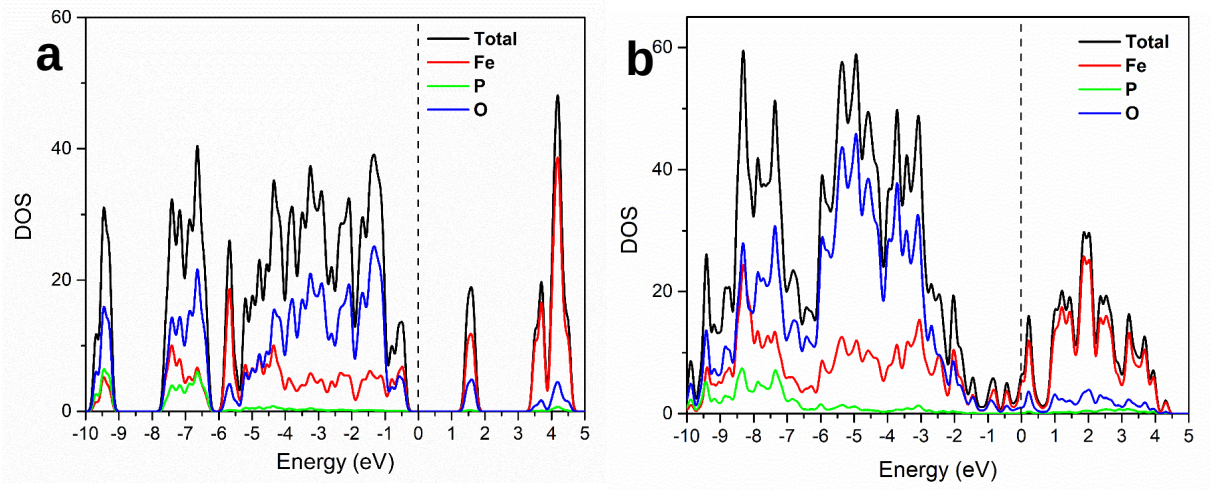

Figure S23 Element-wise PDOS for (a) the bulk $FePO_4$ and (b) the overlayer $FePO_4$ in the FeP/$FePO_4$ heterojunction (the vertical dash-line highlights the location of zero eV)

G. Additional Computational Results on OER Free Energy Profiles

The OER free energy profiles for several surface Fe sites for $FePO_4$ following the 4-electron mechanism and the standard hydrogen electrode model by Nørskov et. al.,[56] in the following steps are computed and the results are summarized in **Figure S23**:

$$OH^+ * \rightarrow *OH + e^- \quad (1)$$

$$*OH \rightarrow *O + H^+ + e^- \quad (2)$$

$$OH^- + *O \rightarrow *OOH + e^- \quad (3)$$

$$*OOH \rightarrow *O_2 + H^+ + e^- \quad (4)$$

$$*O_2 \rightarrow * + O_2 \quad (5)$$

where the * denotes a surface catalytic site, while OH, O, OO, and OOH are surface adsorbates at the surface catalytic site. First, we compared the OER profiles for a 3-coordinate Fe site (as formed from the 2-coordinate Fe from the (010) slab cut via reconstruction) of $FePO_4$ (010) with and without a constraint slab of FeP (**Figure S24a**). The two profiles, denoted by 'FeP/$FePO_4$' and 'FeP' respectively (**Figures S24b-c**), are quite different. The OER for the FeP/$FePO_4$ site has a barrier of 2.75 eV for its rate-limiting *O →*OOH step without any external bias (which equivalently yields a theoretical overpotential of ~1.5 V); the *O species is expected to be the dominant surface species at a bias of 1.23 V. The OER for the $FePO_4$ site has a barrier of 2.0 eV for the rate-limiting *OH → *O step at 0 V (corresponding to a theoretical overpotential of ~0.7 V at 1.23 V), and the surface of the catalyst is likely to be covered by *OH species at 1.23 V. Unfortunately, optimal OER pathways are not found in current study to match the experimental OER performance. Our DFT results, however, suggest that the OER performance of the surface $FePO_4$ can be regulated by the geometrical constraints and, likely, the strains induced by the geometrical constraints. Since various type of lattice mismatches can occur between different facets of FeP and $FePO_4$, there can be a variety of structures available for $FePO_4$ in the surface-

oxidized FeP, which is supported by the amorphous structure of $FePO_4$. In addition, we found that $FePO_4$ contains various sites that provide OER pathways even when the geometrical constraints are not present, which can be in part exemplified by the two additional OER pathways provided by other Fe surface sites on $FePO_4$ (010) (**Figures S24d-f**). The intrinsic versatility in site-wise OER performance may be amplified by the various geometrical constraints and hence give a spectrum of OER performances in the oxidized FeP. It is statistically possible that among all of the possible OER pathways, there are a portion of pathways contribute to the ideal OER performance, i.e. with a ultrasmall overpotential and a low Tafel slope. This is very difficult to prove as it is impractical to predict the OER profiles and hence theoretical overpotentials for all of the possible amorphous $FePO_4$ structures using the first-principle methods. With the current difficulties in explicitly predicting OER performance for the structurally complex OER catalysts, to effectively predict when a new material/catalyst is good or bad for OER, one must seek different computational metrics.

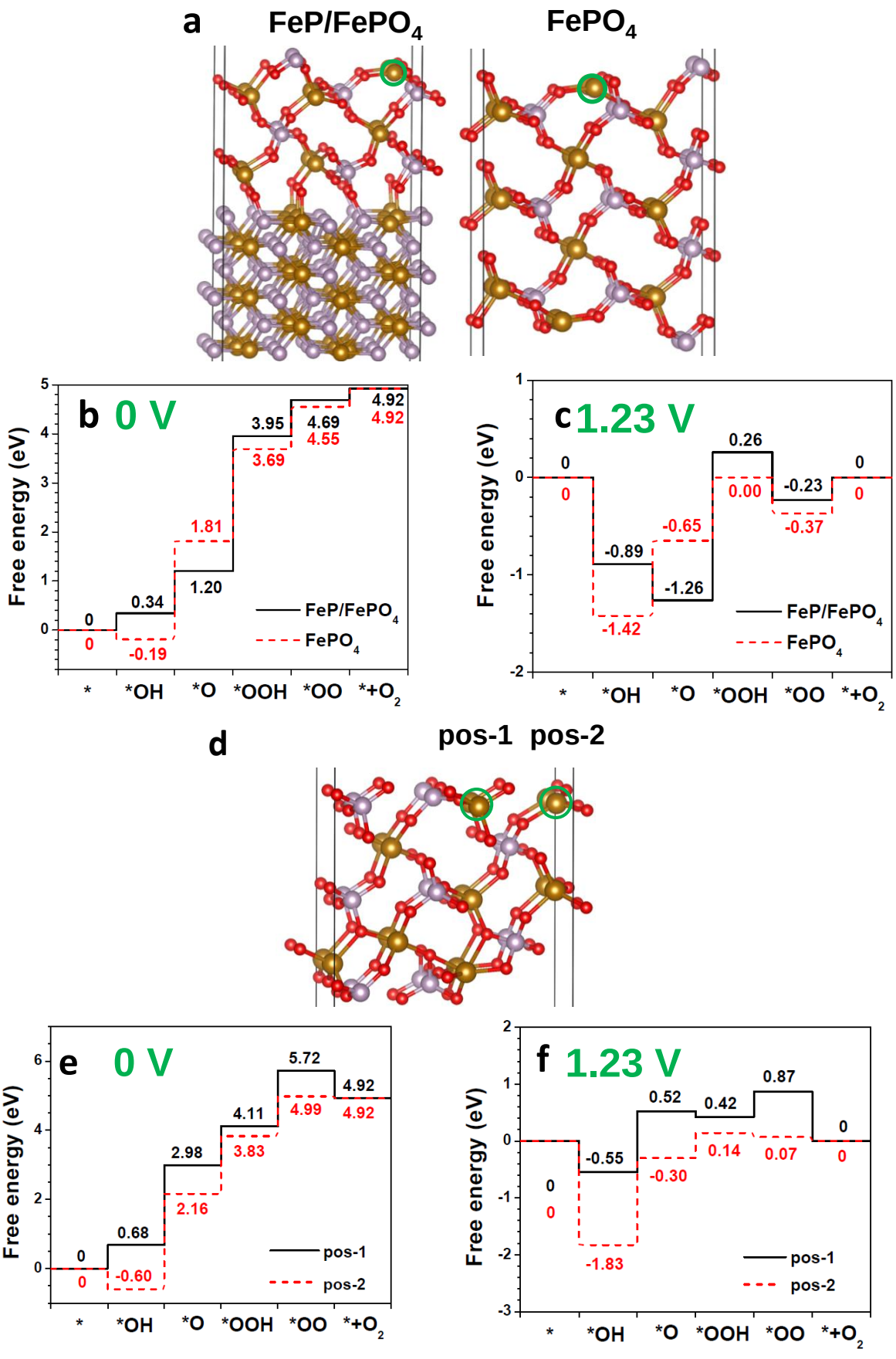
a
FeP/FePO4
FePO4
b 0 V
Free energy (eV)
0
0.34
1.20
1.81
3.95
4.69
4.92
0
-0.19
3.69
4.55
4.92
FeP/FePO4
FePO4
*
*OH
*O
*OOH
*OO
*+O2
c 1.23 V
0
-0.89
-1.26
-0.65
0.26
-0.23
0
0
-1.42
0.00
-0.37
0
d
pos-1
pos-2
e 0 V
0
0.68
2.98
4.11
5.72
4.92
0
-0.60
2.16
3.83
4.99
4.92
pos-1
pos-2
f 1.23 V
0
-0.55
0.52
0.42
0.87
0
0
-1.83
-0.30
0.14
0.07
0

Figure S24 Computational OER free energy profiles at external bias of 0 V and 1.23 V for OER at surface Fe sites of $FePO_4$. **S24a**, b, and **c**: OER profiles for corresponding Fe surface sites of a FeP constrained $FePO_4$ (010) slab (black line) and a free $FePO_4$(010) slab (red dash line). **S24d**, **e**, and **f**: OER profiles for two other Fe surface sites of the free $FePO_4$(010) slab. In the slab structure, Fe atoms are in brown, P atoms are in gray, the O atoms are in red, while the active Fe sites used to create OER profiles are marked with green circles

References for ESI

1. Y. Ha, L. Shi, Z. Chen and R. Wu, *Adv. Sci.*, 2019, **6**, 1900272.
2. F. Yu, H. Zhou, Y. Huang, J. Sun, F. Qin, J. Bao, W. A. Goddard, S. Chen and Z. Ren, *Nat. Commun.*, 2018, **9**, 2551.
3. Q. Lv, L. Yang, W. Wang, S. Lu, T. Wang, L. Cao and B. Dong, *J. Mater. Chem. A*, 2019, **7**, 1196-1205.
4. H. Li, S. Chen, Y. Zhang, Q. Zhang, X. Jia, Q. Zhang, L. Gu, X. Sun, L. Song and X. Wang, *Nat. Commun.*, 2018, **9**, 2452.
5. L. Hui, Y. Xue, B. Huang, H. Yu, C. Zhang, D. Zhang, D. Jia, Y. Zhao, Y. Li and H. Liu, *Nat. Commun.*, 2018, **9**, 5309.
6. Y. Jia, L. Zhang, G. Gao, H. Chen, B. Wang, J. Zhou, M. T. Soo, M. Hong, X. Yan and G. Qian, *Adv. Mater.*, 2017, **29**, 1700017.
7. L. Xiu, Z. Wang, M. Yu, X. Wu and J. Qiu, *ACS nano*, 2018, **12**, 8017-8028.
8. H. Li, Q. Li, P. Wen, T. B. Williams, S. Adhikari, C. Dun, C. Lu, D. Itanze, L. Jiang and D. L. Carroll, *Advanced Materials*, 2018, **30**, 1705796.
9. J. Hou, B. Zhang, Z. Li, S. Cao, Y. Sun, Y. Wu, Z. Gao and L. Sun, *ACS Catalysis*, 2018, **8**, 4612-4621.
10. N. Jiang, B. You, M. Sheng and Y. Sun, *Angewandte Chemie*, 2015, **127**, 6349-6352.

11. M. Ledendecker, S. Krick Calderón, C. Papp, H. P. Steinrück, M. Antonietti and M. Shalom, *Angewandte Chemie International Edition*, 2015, **54**, 12361-12365.

12. G. Zhang, G. Wang, Y. Liu, H. Liu, J. Qu and J. Li, *Journal of the American Chemical Society*, 2016, **138**, 14686-14693.

13. X. Gao, H. Zhang, Q. Li, X. Yu, Z. Hong, X. Zhang, C. Liang and Z. Lin, *Angewandte Chemie*, 2016, **128**, 6398-6402.

14. C. Tang, R. Zhang, W. Lu, L. He, X. Jiang, A. M. Asiri and X. Sun, *Adv. Mater.*, 2017, **29**, 1602441.

15. A. Sivanantham, P. Ganesan and S. Shanmugam, *Advanced Functional Materials*, 2016, **26**, 4661-4672.

16. L. Fan, P. F. Liu, X. Yan, L. Gu, Z. Z. Yang, H. G. Yang, S. Qiu and X. Yao, *Nature communications*, 2016, **7**, 10667.

17. X. Zhang, X. Zhang, H. Xu, Z. Wu, H. Wang and Y. Liang, *Advanced Functional Materials*, 2017, **27**, 1606635.

18. Y. Pan, K. Sun, S. Liu, X. Cao, K. Wu, W.-C. Cheong, Z. Chen, Y. Wang, Y. Li and Y. Liu, *Journal of the American Chemical Society*, 2018, **140**, 2610-2618.

19. R. Lin, H. Lei, D. Ruan, K. Jiang, X. Yu, Z. Wang, W. Mai and H. Yan, *Nano Energy*, 2019, **56**, 82-91.

20. L. M. Cao, Y. W. Hu, S. F. Tang, A. Iljin, J. W. Wang, Z. M. Zhang and T. B. Lu, *Advanced Science*, 2018, **5**, 1800949.

21. X. Wang, W. Ma, C. Ding, Z. Xu, H. Wang, X. Zong and C. Li, *ACS Catalysis*, 2018, **8**, 9926-9935.

22. Y. Hou, Y. Liu, R. Gao, Q. Li, H. Guo, A. Goswami, R. Zboril, M. B. Gawande and X. Zou, *ACS Catalysis*, 2017, **7**, 7038-7042.

23. Z. Xing, C. Han, D. Wang, Q. Li and X. Yang, *ACS Catalysis*, 2017, **7**, 7131-7135.

24. G. F. Chen, T. Y. Ma, Z. Q. Liu, N. Li, Y. Z. Su, K. Davey and S. Z. Qiao, *Advanced Functional Materials*, 2016, **26**, 3314-3323.

25. Q. Qin, H. Jang, P. Li, B. Yuan, X. Liu and J. Cho, *Advanced Energy Materials*, 2018, 1803312.

26. S. Yao, V. Forstner, P. W. Menezes, C. Panda, S. Mebs, E. M. Zolnhofer, M. E. Miehlich, T. Szilvási, N. A. Kumar and M. Haumann, *Chem. Sci.*, 2018, **9**, 8590-8597.

27. F. Wang, X. Yang, B. Dong, X. Yu, H. Xue and L. Feng, *Electrochemistry Communications*, 2018, **92**, 33-38.

28. M. Li, T. Liu, X. Bo, M. Zhou, L. Guo and S. Guo, *Nano Energy*, 2017, **33**, 221-228.

29. W. L. Kwong, E. Gracia‐Espino, C. C. Lee, R. Sandström, T. Wågberg and J. Messinger, *ChemSusChem*, 2017, **10**, 4544-4551.

30. J. Masud, S. Umapathi, N. Ashokaan and M. Nath, *Journal of Materials Chemistry A*, 2016, **4**, 9750-9754.

31. R. Zhang, C. Zhang and W. Chen, *Journal of Materials Chemistry A*, 2016, **4**, 18723-18729.

32. H. Du, S. Gu, R. Liu and C. M. Li, *International Journal of Hydrogen Energy*, 2015, **40**, 14272-14278.

33. Y. P. Zhu, Y. P. Liu, T. Z. Ren and Z. Y. Yuan, *Advanced Functional Materials*, 2015, **25**, 7337-7347.

34. Y. Jin, H. Wang, J. Li, X. Yue, Y. Han, P. K. Shen and Y. Cui, *Advanced Materials*, 2016, **28**, 3785-3790.

35. J. Zhang, T. Wang, D. Pohl, B. Rellinghaus, R. Dong, S. Liu, X. Zhuang and X. Feng, *Angewandte Chemie International Edition*, 2016, **55**, 6702-6707.

36. Y. Hou, M. R. Lohe, J. Zhang, S. Liu, X. Zhuang and X. Feng, *Energy & Environmental Science*, 2016, **9**, 478-483.

37. J. Wang, W. Yang and J. Liu, *Journal of Materials Chemistry A*, 2016, **4**, 4686-4690.

38. L. Yu, H. Zhou, J. Sun, F. Qin, F. Yu, J. Bao, Y. Yu, S. Chen and Z. Ren, *Energy & Environmental Science*, 2017, **10**, 1820-1827.

39. Y. Lian, H. Sun, X. Wang, P. Qi, Q. Mu, Y. Chen, J. Ye, X. Zhao, Z. Deng and Y. Peng, *Chemical science*, 2019, **10**, 464-474.

40. L. Yu, Y. Xiao, C. Luan, J. Yang, H. Qiao, Y. Wang, X. Zhang, X. Dai, Y. Yang and H. Zhao, *ACS applied materials & interfaces*, 2019, **11**, 6890-6899.

41. T. Tang, W.-J. Jiang, S. Niu, N. Liu, H. Luo, Y.-Y. Chen, S.-F. Jin, F. Gao, L.-J. Wan and J.-S. Hu, *Journal of the American Chemical Society*, 2017, **139**, 8320-8328.

42. P. Babar, A. Lokhande, H. Shim, M. Gang, B. Pawar, S. Pawar and J. H. Kim, *Journal of Colloid and Interface Science*, 2019, **534**, 350-356.

43. A.-L. Wang, H. Xu and G.-R. Li, *ACS Energy Letters*, 2016, **1**, 445-453.

44. S. Wei, K. Qi, Z. Jin, J. Cao, W. Zheng, H. Chen and X. Cui, *Acs Omega*, 2016, **1**, 1367-1373.

45. L. Yan, H. Jiang, Y. Xing, Y. Wang, D. Liu, X. Gu, P. Dai, L. Li and X. Zhao, *Journal of Materials Chemistry A*, 2018, **6**, 1682-1691.

46. J. Wu, X. Chong, R. Zhou, Y. Jiang and J. Feng, *RSC Adv.*, 2015, **5**, 81943-81956.

47. G. Bhalerao, P. Hermet, J. Haines, O. Cambon, D. Keen, M. Tucker, E. Buixaderas and P. Simon, *Physical Review B*, 2012, **86**, 134104.

48. P. Tang and N. Holzwarth, *Physical Review B*, 2003, **68**, 165107.

49. G. Kresse and J. Furthmüller, *Phys. Rev. B*, 1996, **54**, 11169.

50. G. Kresse and J. Furthmüller, *Comp. Mater. Sci.*, 1996, **6**, 15-50.

51. G. Kresse and D. Joubert, *Phys. Rev. B*, 1999, **59**, 1758.

52. J. P. Perdew, K. Burke and M. Ernzerhof, *Phys. Rev. Lett.*, 1996, **77**, 3865.

53. S. Grimme, J. Antony, S. Ehrlich and H. Krieg, *J. Chem. Phys.*, 2010, **132**, 154104.

54. H. J. Monkhorst and J. D. Pack, *Phys. Rev. B*, 1976, **13**, 5188.

55. J. Heyd, G. E. Scuseria and M. Ernzerhof, *The Journal of chemical physics*, 2003, **118**, 8207-8215.

56. J. K. Nørskov, T. Bligaard, A. Logadottir, J. Kitchin, J. G. Chen, S. Pandelov and U. Stimming, *Journal of the Electrochemical Society*, 2005, **152**, J23-J26.